J. Fluid Mech. (2000), *vol.* 416, *pp.* 315–348. Printed in the United Kingdom

© 2000 Cambridge University Press

Formation of sand bars under surface waves

By JIE YU AND CHIANG C. MEI

Department of Civil and Environmental Engineering,
Massachusetts Institute of Technology, Cambridge, MA 02139, USA

(Received 4 November 1999 and in revised form 28 March 2000)

A quantitative theory is described for the formation mechanism of sand bars under surface water waves. By assuming that the slopes of waves and bars are comparably gentle and sediment motion is dominated by the bedload, an approximate evolution equation for bar height is derived. The wave field and the boundary layer structure above the wavy bed are worked out to the accuracy needed for solving this evolution equation. It is shown that the evolution of sand bars is a process of forced diffusion. This is unlike that for sand ripples which is governed by an instability. The forcing is directly caused by the non-uniformity of the wave envelope, hence of the wave-induced bottom shear stress associated with wave reflection, while the effective diffusivity is the consequence of gravity and modified by the local bed stress. During the slow formation, bars and waves affect each other through the Bragg scattering mechanism, which consists of two concurrent processes: energy transfer between waves propagating in opposite directions and change of their wavelengths. Both effects are found to be controlled locally by the position of bar crests relative to wave nodes. Comparison with available laboratory experiments is discussed and theoretical examples are studied to help understand the coupled evolution of bars and waves in the field.

1. Introduction

Two morphological features are commonly found on the seabed near the shore: sand ripples with typical amplitudes of a few centimeters and wavelengths a few tens of centimetres, and sand bars of much greater height and wavelength. Records of sand bars by aerial photography or by acoustic sounding have been reported by many, including Kindle (1936) and Dolan (1983) for Chesapeake Bay, Evans (1940) and Saylor & Hands (1947) for Lake Michigan, Lau & Travis (1973) for Escambia Bay, Florida, Sheppard (1950) for Southern California and Short (1975) for the Alaskan Arctic. The typical slope of these beaches is small ($< 5\%$). The number of bars ranges from a few to a few tens while the spacing varies widely from a few metres in bays to several hundreds of metres along an open coast.

Effects of sand bars on the wave climate of the coast and the processes which generate them are of both scientific and engineering interest. While no single mechanism governs all cases, several rather distinct mechanisms have been suggested. Evans (1940) was the first to point out that the first bar can be formed on an initially plane sloping beach by the falling crests of plunging breakers, which can excavate sand particles directly beneath and then deposit them slightly seaward of the breaker line. The effectiveness of this process was confirmed by Keulegan's (1948) laboratory study (commissioned by the US Army in preparation for the landing of Allied Troops at Normandy in the second World War).

In laboratory experiments, Herbich, Murphy & Van Weele (1965) have shown that near a reflecting seawall bars can form at the spacing of half the incident wavelength. Analysing the boundary layer above a rigid bed for moderate surface wavelengths, Carter, Liu & Mei (1973) have found that the wave-induced drift current forms circulating cells when the reflection coefficient exceeds 0.414. Close to the bed, the drift is directed towards the points beneath the nodes (or envelope minima) and away from the antinodes (or envelope maxima); at the outer edge of the boundary layer, the drift is oppositely directed. By observing a monolayer of sand on the rigid bottom of a flume under strongly reflected waves, they have found that large particles which tend to roll and slide on the bottom accumulate beneath the envelope nodes, again spaced half a surface wavelength apart. Based on these results, Carter *et al.* suggest that the cellular drift, which requires strong reflection, is the key to the formation of half-wavelength bars.

However, half-wavelength bars have also been observed over a thick layer of sand by O'Hare & Davies (1990) and Rey, Davies & Belzons (1995) under weakly reflected waves. In particular, O'Hare & Davies point out that the spatial variation of the mass transport velocity due to wave reflection may be sufficient to produce convergence and divergence of sediments with half-wavelength spacing, whether or not there are circulating cells. To simulate their laboratory experiments, O'Hare & Davies (1993) later proposed a computational model of sand bar evolution in constant mean water depth under reflected waves. The wave field is computed numerically by discretizing the bed surface as a number of horizontal steps. Two sediment transport models were considered: suspended load and vortex load, which accounts for suspensions in vortices shed over ripples. The two modes of transport are assumed to be distinguishable and can be described by the empirical formulas of Nielsen (1979, 1981, 1986, 1988). They find that half-wavelength sand bars are formed with the position of the bar crests depending on which of the two modes of suspension is more important.

For long waves in shallow water, higher harmonics are generated by nonlinearity and can introduce a much longer scale of spatial modulation (or recurrence, see Mei & Ünlüata 1972; Lau & Barcilon 1972). Boczar-Karakiewicz, Paplinska & Winiecki (1981) have studied experimentally sand bars as long as the recurrence length. A theoretical model for bars generated by such long waves has been proposed by Boczar-Karakiewicz, Bona & Cohen (1987) based on the Boussinesq equations. Sediment is assumed to be transported in suspension by the mass transport velocity inside the boundary layer. Essentially the same approach has been employed by Restrepo & Bona (1995) to include three-dimensional effects as well as internal waves.

While wave reflection can initiate bars on a flat erodible bed, changes in waves must also occur when the bars grow to sufficient height. By experiments with rigid bars in a long wave flume, Heathershaw (1982) has first demonstrated that many gently sloped bars spaced at half the length of the incident waves can cause strong reflection by constructive interference. The linear aspects of this mechanism of Bragg resonance have since been studied theoretically by many authors for rigid bars (e.g. Davies & Heathershaw 1984; Mei 1985; Kirby 1986; Liu 1987; Belzons, Rey & Guazzelli 1991; Yu & Mei 2000). Nonlinear effects of rigid bars on waves have also been examined by Mei (1985), Hara & Mei (1987) and Yoon & Liu (1987).

This paper is aimed at improving our understanding of the formation mechanism of sand bars and their interaction with waves in the shoaling zone where breaking is absent and waves are gentle. In particular we wish to discern whether the bars are formed by an instability mechanism, as are sand ripples (Blondeaux 1990; Vittori &

Blondeaux 1990; see also Mei & Yu 1997), and how Bragg resonance of waves may be affected. Attention is restricted to cases where ripples, if any, have much smaller amplitudes than sand bars, as shown in the acoustic sounding records taken from Chesapeake Bay by Dolan (1983), and hence can be treated as the bottom roughness affecting the estimate of the eddy viscosity. Our model presumes coarse sand† and weak waves so that sediment is mainly transported as bedload.

In § 2, the basic assumptions are detailed. The sediment continuity equation which describes the changes of the bottom is then presented in § 3, complemented by an empirical bedload formula which relates the sediment transport rate to the bed shear stress. In § 4, we derive formally the evolution equation of the bar height and determine the extent of information needed from the fluid flow, which is then obtained in § 5. After discussions of the physical properties of the bar evolution equation and the steady-state bar profile in terms of the local wave intensity (§§ 6, 7), the numerical procedure for the coupled evolution of bars and waves is outlined (§ 8). Comparison with available laboratory experiments then is made in § 9. The coupled process of Bragg scattering and bar evolution is studied in § 10 and § 11. Comments on the distinctions between bars and ripples and on the similitude in laboratory experiments are made at the end.

2. Assumptions

We consider monochromatic gravity waves propagating over water of constant mean depth H. Let K, A_0 and ω represent the typical wavenumber, free-surface amplitude and angular frequency of surface waves respectively, while K_b and D are the typical wavenumber and amplitude of sand bars. For convenience the characteristic horizontal orbital amplitude of wave oscillations just above the bed

$$A_b = \frac{A_0}{\sinh(KH)} \tag{2.1}$$

will be taken as the amplitude scale.

Attention will be confined to the shoaling zone where the wavelengths of sand bars and surface waves are comparable to the water depth, i.e.

$$KH = O(1), \qquad \frac{K_b}{K} = O(1). \tag{2.2}$$

The slopes of both surface waves and sand bars will be assumed to be gentle and characterized by the small parameter ϵ,

$$\epsilon \equiv A_b K = O(DK_b) \ll 1, \tag{2.3}$$

Sand bars are often covered by small sand ripples which are formed much more quickly than bars. The height of ripples ($2a_{rip}$) is typically a few centimetres in the field, while that of bars ($2D$) can be a few tens of centimetres to a few metres. This contrast can be seen from the field records of Dolan (1983) and the laboratory records of Boczar-Karakiewicz *et al.* (1981). On the other hand, it is also known from observations in the field and in the laboratory that the ripple wavelength $2\pi/k_{rip}$ is comparable to A_b, the wave orbital amplitude near the bottom, which is of $O(10\,\text{cm})$ (see Van Rijn 1993, p. 5.38). It is therefore reasonable to assume small ripple steepness, i.e. $k_{rip}a_{rip} \ll 1$, which can also be deduced from (2.2) and (2.3) with

† Sleath (1984, p. 110) classifies the sands by their diameters as follows: very fine 0.062–0.0125 mm, fine 0.125–0.25 mm, medium 0.25–0.5 mm, coarse 0.5–1.0 mm, very coarse 1–2 mm.

$a_{rip} \ll D$ and $A_b k_{rip} = O(1)$. It has been shown before that the ripple-induced flow is of the order $(k_{rip}a_{rip})\omega A_b$, which has the spatial period of $2\pi/k_{rip}$ (Sleath 1974; Blondeaux 1990; Mei & Yu 1997). Upon averaging over the ripple length the net effect of this induced flow vanishes at the second order in surface wave slope and should not affect significantly the bedload transport over the scale of a bar length. By extending Trowbridge & Madsen (1984*a*, *b*), Davies & Villaret (1999) modelled the effects of non-erodible ripples by treating a theoretically flat bed and an eddy viscosity periodic in space and time. The results on mass transport differ qualitatively from earlier models of constant or depth-dependent eddy viscosity (Longuet-Higgins 1953) only at the upper edge of the boundary layer but not near the bed. In our theory we shall ignore the detailed hydrodynamics on the scale of ripples, but account for their presence as a roughness which affects the turbulent eddy viscosity of the mean flow. The surface of the seabed is here taken to be the mean surface averaged over ripples. Unlike Davies & Villaret we shall assume for analytical expediency a constant eddy viscosity, ν, which is estimated from the wave characteristics and sand diameter through an empirical procedure known in coastal engineering and summarized in Appendix A.

To give some quantitative idea, we find for a typical wave period of $T = 8\,\mathrm{s}$, water depth $H = 7\,\mathrm{m}$ and sand diameter $d = 0.4\,\mathrm{mm}$, and for two incident wave amplitudes $A_0 = (25, 50)\,\mathrm{cm}$, the eddy viscosity to be $\nu = (4.79, 15.36)\,\mathrm{cm^2\,s^{-1}}$. The corresponding boundary layer thickness is of the order $\delta = \sqrt{2\nu/\omega} = (3.50, 6.26)\,\mathrm{cm}$, which is much smaller than the typical surface wavelength. For convenience in the perturbation analysis we shall take specifically

$$K\delta = O(\epsilon^2). \tag{2.4}$$

It then follows that

$$O\left(\frac{A_b}{\delta}\right) = O\left(\frac{D}{\delta}\right) = O(\epsilon^{-1}). \tag{2.5}$$

As will be shown shortly, an important parameter in the empirical laws of sediment transport is the sand diameter d, which will be assumed to be

$$d/\delta = O(\epsilon) \ll 1. \tag{2.6}$$

3. Sediment transport rate and local flow

The complex dynamics of the sand/water mixture has so far been described only empirically. It is customary to supplement the kinematic law of mass conservation by an empirical relation between the sediment discharge rate and the local shear stress. In physical dimensions, let q' denote the volume discharge rate, h' the bottom profile averaged over small ripples and measured from the mean position of the bottom, and n the bed porosity, then conservation of sediment requires that

$$(1-n)\frac{\partial h'}{\partial t'} + \frac{\partial q'}{\partial x'} = 0. \tag{3.1}$$

Primes are used here to denote variables with physical dimensions. In general, sediment transport can be composed of both suspended loads and bedloads. Outside the surf zone, the shear stress can be weak enough so that the bedload, whereby sand particles roll and hop in a very thin layer, is dominant. From experiments for steady flows, Fredsøe & Deigaard (1992) have suggested that particles are suspended if

$$w_s' < Cu_*', \tag{3.2}$$

where w_s' is the settling velocity and u_*' is the friction velocity defined by $u_*' = \sqrt{f_w/2}A_b\omega$; the wave friction factor f_w is calculated from the empirical recipe in Appendix A with the bed roughness chosen to be 2.5 times the particle diameter. The coefficient C is 1 according to Bagnold (1966) and 0.8 according to Fredsøe & Deigaard (1992). For the examples cited in § 2, $u_*' = (2.10, 3.01)\,\mathrm{cm\,s^{-1}}$. Then the particle diameter must be smaller than 0.2 mm (fine and very fine sand according to Sleath's classification) for suspended load to be significant. Thus, our theory is limited to medium or coarse sand, or weak waves.

For spatially uniform oscillatory flows, Sleath (1978) has performed experiments for a uniform sand layer on a horizontal plate at the bottom of a water layer. Sediment movement was generated by oscillating sinusoidally the bottom plate in its own plane at the velocity $U' \propto \cos\omega t'$. Once moved, most of the sediment remained in motion throughout subsequent cycles even when the flow intensity fell temporarily below the threshold of the incipient sand motion. As a result the transport rate is described by a continuous rather than an intermittent function of time, as follows:

$$q' = \tfrac{8}{3}Q_s'\cos^4(\omega t' + \Delta\varphi)\mathrm{sgn}\,[\cos(\omega t' + \Delta\varphi)] \propto U'^4\mathrm{sgn}\,(U'), \tag{3.3}$$

where Q_s' is the mean discharge averaged over half a cycle and depends on the maximum shear stress $\widehat{\tau}_b'$. The phase difference $\Delta\varphi$ between the transport rate and the fluid velocity U just outside the bed boundary layer has values of 10°–20°.

For uniform flows over a horizontal bed, various formulas have been proposed to relate Q_s' to the maximum bottom shear stress $\widehat{\tau}_b'$. It is customary in sediment dynamics to use the Shields parameter,

$$\Theta = \frac{\tau_b'}{\rho(s-1)gd}, \tag{3.4}$$

which is the ratio of shear-induced fluid force on a grain to the buoyant weight of the grain. By examining data from several investigators, both Sleath (1982) and Nielsen (1992) have suggested that Q_s' takes the following form:

$$\frac{Q_s'}{\sqrt{(s-1)gd^3}} = \begin{cases} C_s(\widehat{\Theta} - \Theta_c)^{1.5}, & \widehat{\Theta} > \Theta_c \\ 0, & \widehat{\Theta} < \Theta_c. \end{cases} \tag{3.5}$$

Here C_s is an empirical constant, $\widehat{\Theta}$ and Θ_c are the maximum and critical Shields parameters, related respectively to the maximum $\widehat{\tau}_b'$ and critical $\widehat{\tau}_c'$ bed shear stresses via (3.4). The constant in (3.5) is taken to be $C_s = 1.95$ by Sleath and $C_s = 3$ by Nielson; the difference is a reflection of the data scatter.

Since the flow in Sleath's experiments was turbulent, we invoke the usual empirical relation that $\tau_b' \propto |U'|U'$ and rewrite his formula in terms of an equivalent sinusoidal bed shear stress,†

$$\tau_b'(t) = \widehat{\tau}_b|\cos(\omega t' + \Delta\varphi)|\cos(\omega t' + \Delta\varphi), \tag{3.6}$$

so that

$$q' = \tfrac{8}{3}Q_s'\left(\frac{\Theta(\omega t' + \Delta\varphi)}{\widehat{\Theta}}\right)^2 \mathrm{sgn}\,[\Theta(\omega t' + \Delta\varphi)]. \tag{3.7}$$

It will be shown later that the phase angle $\Delta\varphi$ is immaterial after taking time averages.

Note that the empirical formulae (3.3) and (3.7) are for a horizontal sandy bed. On

† In the thesis by Yu (1999), calculations have also been made by assuming the sediment transport rate to be proportional to the fourth power of the bed shear stress. The results are not significantly different.

a sloping sandy surface, particles tend to move downhill due to gravity, therefore the driving force for sediment motion must be the vector sum of bed shear stress and the gravitational force. In his study of river bars induced by steady flows, Fredsøe (1974) has proposed extending the bedload discharge formula by replacing the Shields parameter with

$$\Theta = \frac{\tau_b'}{\rho(s-1)gd} - \beta\frac{\partial h'}{\partial x'} \tag{3.8}$$

which will be called the *modified* Shields parameter here, where $\beta = O(\Theta_c/\tan\phi_s)$ and ϕ_s is the angle of repose. From the Shields diagram (e.g. Sleath 1984, p. 260), Θ_c is about 0.05 for medium size sand and $\phi_s = O(30^\circ)$ typically, hence $\beta \sim O(0.1)$. While no comprehensive data on β are available, this modification is heuristically reasonable and has been employed for modelling bars in rivers (Fredsøe 1974), and ripples in oscillatory flows (Blondeaux 1990; Vittori & Blondeaux 1990; Mei & Yu 1997).

Under the action of partially standing surface waves, the shear stress varies with x' as well as with t'. We shall assume in addition that the local behaviour of $q'(x', t')$ for a given x' is related to the local shear stress by (3.7). In summary, the sand transport formula under partially standing surface waves is taken to be

$$q'(x', t') = \tfrac{8}{3}Q_s'(x')\left\{\frac{\Theta(Kx', \omega t' + \Delta\varphi)}{\widehat{\Theta}(Kx')}\right\}^2 \operatorname{sgn}\left[\Theta(Kx', \omega t' + \Delta\varphi)\right], \tag{3.9}$$

where the modified Shields parameter is defined by

$$\Theta(Kx', \omega t' + \Delta\varphi) = \frac{\tau_b'(x', t' + \Delta\varphi/\omega)}{\rho(s-1)gd} - \beta\frac{\partial h'}{\partial x'} \tag{3.10}$$

with $\widehat{\Theta}(Kx')$ denoting the local maximum of Θ and

$$\frac{Q_s'(x')}{\sqrt{(s-1)gd^3}} = \begin{cases} C_s[\widehat{\Theta}(Kx') - \Theta_c]^{1.5}, & \widehat{\Theta}(Kx') > \Theta_c \\ 0, & \widehat{\Theta}(Kx') < \Theta_c. \end{cases} \tag{3.11}$$

When (3.9) is substituted into (3.1), with the bed shear stress being computed from the known flow field (cf. § 5), an evolution equation for h' can be obtained.

Since the original sediment transport relation was obtained from experiments in uniform flows over flat beds, its application must be limited to cases where the local spatial gradient is small. As will be seen later there are small neighbourhoods where the predicted bed slope is large; our solution there can only suggest the possibility of local avalanches, and should be corrected by a more accurate model of granular dynamics. The remedy of these local shortcomings is however beyond our present knowledge of sediment mechanics and will not be attempted.

We now utilize the presence of the small parameter ϵ to seek more explicit approximations.

4. Approximate evolution equation of sand bars

In view of (3.9) and (3.11), the magnitude of the transport rate is

$$q' \sim O(\sqrt{(s-1)gd^3}\,\widehat{\Theta}^{1.5}). \tag{4.1}$$

Because of the gentle slope of the sand bars, the total Shields parameter (3.10) is dominated by the first term, i.e. the plane-bed Shields parameter, whose order of

magnitude can be estimated as

$$O(\widehat{\Theta}) \sim \frac{A_b \omega v}{(s-1)gd\delta} \equiv \Theta_0. \tag{4.2}$$

Introducing the following dimensionless variables:

$$q' = \frac{8C_s}{3}\sqrt{(s-1)gd^3}\Theta_0^{1.5} q, \quad h' = A_b h, \quad t' = \frac{t}{\omega}, \quad x' = \frac{x}{K}, \tag{4.3}$$

we write (3.1) in the dimensionless form

$$(1-n)\frac{\alpha}{\Theta_0^{1.5}}\frac{\partial h}{\partial t} + \frac{\partial q}{\partial x} = 0, \tag{4.4}$$

where α is another dimensionless parameter,

$$\alpha = \frac{3}{8C_s}\frac{A_b\omega}{K\sqrt{(s-1)gd^3}}. \tag{4.5}$$

The ratio $\alpha/\Theta_0^{1.5}$ is the dimensionless time scale normalized by ω^{-1}. Under the assumptions made in § 2, $\Theta_0 = O(1)$ and $\alpha = O(\epsilon^{-3.5})$, this ratio is very large. It follows that at the leading order h does not vary significantly over a few wave periods. Denoting period averages by overbars, we get from (4.4) that

$$(1-n)\frac{\alpha}{\Theta_0^{1.5}}\frac{\partial \bar{h}}{\partial t} + \frac{\partial \bar{q}}{\partial x} = 0. \tag{4.6}$$

The part of q that oscillates at the wave frequency contributes to a small correction to $\bar{h}$.

We now seek approximations for small ϵ. As will be explained more fully in the next section, it is convenient to use a vertical coordinate $\eta' = z' - \bar{h}' = \delta\eta$ measured from the bar surface, and the stream function $\psi'(x', \eta', t')$ for the flow in the boundary layer. Because of (2.4) and the gentle slope of the bars, the tangential shear stress on the bed is $\tau_b' = \rho\nu\partial^2\psi'/\partial\eta'^2 + O(\epsilon^2)$ at $\eta' = 0$. By expanding the normalized stream function, $\psi = \psi'/(A_b\omega\delta)$, in powers of ϵ, i.e. $\psi = \psi_0 + \epsilon\psi_1 + \cdots$, the instantaneous modified Shields parameter (3.10) can be approximated as

$$\Theta = \Theta_0\frac{\partial^2\psi_0}{\partial\eta^2} + \epsilon\left(\Theta_0\frac{\partial^2\psi_1}{\partial\eta^2} + \beta\frac{\partial h}{\partial x}\right) + O(\epsilon^2) \quad \text{on } \eta = 0. \tag{4.7}$$

Expanding the discharge rate similarly, $q = q_0 + \epsilon q_1 + \epsilon^2 q_2 + \cdots$, and taking the time average, we get from (3.9), after some algebra (see Appendix B),

$$\bar{q}_0 = 0, \qquad \bar{q} = \epsilon\bar{q}_1, \tag{4.8}$$

with

$$\bar{q}_1 = 2Q_{s0}\frac{\overline{|\psi_{0,\eta\eta}|(\psi_{1,\eta\eta} - (\beta/\Theta_0)h_x)}}{(\widehat{\psi_{0,\eta\eta}})^2} \tag{4.9}$$

where

$$Q_{s0} = \begin{cases} (\widehat{\psi_{0,\eta\eta}} - \Theta_c/\Theta_0)^{1.5}, & \widehat{\psi_{0,\eta\eta}} > \Theta_c/\Theta_0 \\ 0, & \widehat{\psi_{0,\eta\eta}} \leqslant \Theta_c/\Theta_0 \end{cases} \tag{4.10}$$

is, in dimensionless form, the leading-order approximation of Q_s' in (3.11). Here $\widehat{\psi_{0,\eta\eta}}$ denotes the amplitude of $\psi_{0,\eta\eta}$.

We now substitute (4.8) into (4.6), and introduce a renormalized time,

$$\bar{t} = \frac{\epsilon \Theta_0^{1/2}}{\alpha} t. \tag{4.11}$$

The result is the normalized evolution equation for the bar height $\bar{h}$ to the leading order:

$$\frac{\partial \bar{h}}{\partial \bar{t}} - \frac{\partial}{\partial x}\left(D_v \frac{\partial \bar{h}}{\partial x}\right) = -\frac{\partial q_\tau}{\partial x}, \tag{4.12}$$

where

$$D_v = \frac{2\beta}{1-n} Q_{s0} \frac{\overline{|\psi_{0,\eta\eta}|}}{(\widehat{\psi_{0,\eta\eta}})^2} \tag{4.13}$$

and

$$q_\tau = \frac{2\Theta_0}{1-n} Q_{s0} \frac{\overline{|\psi_{0,\eta\eta}|\psi_{1,\eta\eta}}}{(\widehat{\psi_{0,\eta\eta}})^2}. \tag{4.14}$$

Together with (4.13) and (4.14), equation (4.12) is a key result of this study.

As will become clear in the next section, D_v and q_τ do not depend on the bar height $\bar{h}$. Therefore, the evolution of sand bars is a diffusion process forced by the wave-induced bed stresses, with both diffusivity and forcing depending on the local boundary layer flow. This mechanism differs markedly from the instability mechanism of ripple generation, owing to the sharp differences of wavelength ratios (ripple/surface wave and bar/surface wave), cf. § 12. Note in particular that the diffusivity owes its presence to the downward pull of particles by gravity and prevents unbounded growth of bar crests by the fluid shear. In addition, the following remarks can be made.

(*a*) From (4.11), the time scale of bar growth is $O(\epsilon^{-4.5}\omega^{-1})$, and much longer than that of the wave envelope evolution due to Bragg scattering, which is known to be $O(\epsilon^{-1}\omega^{-1})$ (Mei 1985). For convenience of comparison we shall regard $\epsilon^{-1}\alpha/\Theta_0^{1/2} = \epsilon^{-a}$, and $\bar{t} = \epsilon^a \omega t'$, with $a = 4.5$.

(*b*) Because of the gentle slope of sand bars, the bar-induced flow is $O(\epsilon)$. The oscillatory boundary layer flow to the leading order is just the Stokes solution in the boundary-fitting coordinates (x, η). In particular, ψ_0 consists of only the first time harmonic ($e^{\pm i\omega t'}$) for monochromatic surface waves. Since $|\psi_{0,\eta\eta}|$ can only have even harmonics in time, all the odd time harmonics of ψ_1 are not needed to compute q_τ from (4.14). This observation greatly simplifies the otherwise laborious analysis of the flow field.

(*c*) Since we are interested in many bars and Bragg resonance, the flow field contains two contrasting length scales and will be described in terms of two coordinates, x and $x_1 = \epsilon x$. Anticipating that bars are nearly periodic with slow modulation, we can apply the multiscale expansion to (4.12). Let $\bar{h} = \bar{h}_0(x, x_1, \bar{t}\,) + \epsilon \bar{h}_1(x, x_1, \bar{t}\,) + \cdots$, where $\bar{h}_0, \bar{h}_1, \ldots$ are periodic in the bar scale x. At the leading order, we get from (4.12),

$$\frac{\partial \bar{h}_0}{\partial \bar{t}} + \frac{\partial \bar{q}}{\partial x} = 0, \tag{4.15}$$

where

$$\bar{q} = q_\tau(x, x_1, \bar{t}) - D_v(x, x_1, \bar{t}) \frac{\partial \bar{h}_0}{\partial x}. \tag{4.16}$$

Clearly, because of the periodicity of the flow, q_τ, D_v and $\bar{h}_0$ should be periodic in the

bar scale x. By taking the spatial average, denoted by angle brackets, of (4.15) over a bar length, $\langle \bar{h}_0 \rangle$ is shown to be constant in $\bar{t}$, hence zero for an initially flat bed. It follows that $\langle \bar{h} \rangle = \epsilon \langle \bar{h}_1 \rangle$, which can be found by taking the spatial average of the next order approximation,

$$\frac{\partial \langle \bar{h}_1 \rangle}{\partial \bar{t}} + \frac{\partial \langle \bar{q} \rangle}{\partial x_1} = 0. \tag{4.17}$$

Since we are only interested in the leading order of h, i.e. $\bar{h}_0$, we shall from now on use h to represent $\bar{h}_0$. Let us now turn to the flow field in order to obtain the bottom shear stress.

5. The fluid flow

As before we let all physical variables be distinguished by primes. Within the model of constant eddy viscosity, the fluid velocity (u', w') and the pressure p' in the vertical plane (x', z') are governed by the Navier–Stokes equations, omitted here for brevity.

5.1. *Boundary conditions on the bar surface*

Let us first assess the possible effects of the sand movement on the fluid velocity on the bar surface. Since the time scale of the bar evolution is $O(\epsilon^{-a}\omega^{-1})$ with $a = 4.5$, the normal velocity of the bar surface is at most $O(\epsilon^a \omega h') = O(\epsilon^a \omega A_b)$, and is negligible to the order of interest, i.e. $O(\epsilon \omega A_b)$. Thus, we impose

$$-u' h'_{x'} + w' = O(\epsilon^4 \omega A_b) \quad \text{on } z' = h'(x', t'). \tag{5.1}$$

Now we consider the tangential velocity component. From either visual observations in the laboratory, or by estimates according to the bedload transport formulae, the thickness of the moving sand layer is comparable to a few sand diameters d. Therefore the tangential velocity of the sand layer can only be of the magnitude $u'_s = O(d/\delta) A_b \omega$. Since $d/\delta = O(\epsilon)$, we conclude that u'_s, hence the boundary value of u', can only be of the magnitude $O(\epsilon A_b \omega)$ at most. To the leading order the velocities in the inviscid zone have only the first time harmonic. Thus, the even harmonic components of u'_s can at most be $O(\epsilon^2 A_b \omega)$, i.e.

$$\{u' + w' h'_{x'}\}^{[0],[2]} = O(\epsilon^2 A_b \omega) \quad \text{on } z' = h'(x', t'), \tag{5.2}$$

where $\{\cdot\}^{[n]}$ denotes the nth time harmonic of the quantity inside the brackets. Because the bars are gentle in slope, (5.1) and (5.2) together imply that the vertical velocity and the even harmonics of the horizontal velocity on the bottom can at most be $O(\epsilon^2 A_b \omega)$.† These boundary conditions provide sufficient information for computing D_v and q_τ in the diffusion equation (4.12), since q_τ depends only on the even harmonics of $\epsilon \psi_1$.

We can further confirm the above estimate of the thickness of the moving sand layer. From (3.9) the sand transport rate along the bed is estimated to be $q' = O(Q'_s) \sim \sqrt{(s-1) g d^3} \Theta_0^{1.5}$. Let the sediments in the moving layer of thickness l' be carried by the velocity u'_s whose magnitude is comparable to the fluid velocity averaged over the depth of this layer. Then $u'_s \sim A_b \omega l' / 2\delta$, and the sediment flux rate in this layer is

† On the bed, the first time harmonic of the tangential velocity can still be $O(\epsilon A_b \omega)$, but this affects neither q_τ nor D_v.

$q' \sim u_s' l'(1-n)$. It follows that

$$\frac{l'}{\delta} \sim \sqrt{\frac{2(A_b\omega)^{0.5}\nu^{1.5}}{(s-1)g(1-n)\delta^{2.5}}}. \tag{5.3}$$

For numerical estimates, let us take the typical wave conditions and sand diameter used in § 2. Then $\epsilon = (0.033, 0.066)$, $\nu = (4.79, 15.36)\,\mathrm{cm^2\,s^{-1}}$ (Appendix A). $l'/\delta = (0.065, 0.089)$ and are indeed very small. Thus, $u_s' = (0.028, 0.045)A_b\omega$, or $u_s' = O(\epsilon A_b\omega)$, as estimated before. Recent experiments by Zala Flores & Sleath (1998) in a high-velocity oscillating water tunnel show that the mobile layer thickness of a *sheet flow*, where the top layer of grains is moved appreciably by water, is three times the local Shields parameter times the grain diameter (their equation (5)). For the present study the relevant range of Shields parameter is of order unity, hence our estimate is consistent with their empirical finding.

The free surface is assumed to be free of wind stress, so that the usual kinematic boundary condition and the stress-free conditions apply. The water region can then be divided into the inviscid core and the boundary layer.

5.2. *Inviscid Core*

In the core region above the bed, the representative length scale is the water wavelength $2\pi/K$. The ratio of viscous terms to acceleration is of the order

$$\frac{\nu\nabla'^2 u'}{u_{t'}'} = O\left(\frac{K^2\nu}{\omega}\right) = O(K\delta)^2 = O(\epsilon^4). \tag{5.4}$$

On the free surface, all terms in the tangential stress condition are at most $O(\epsilon^3)$ relative to the dynamic pressure, hence ineffective. Thus, the core region is inviscid up to the order of interest. Assuming irrotationality, the flow field can be described by a velocity potential Φ' such that $(u', w') = \nabla'\Phi'$.

We now introduce the following normalized variables according to scales pertinent to the inviscid core:

$$\Phi = \frac{K}{A_b\omega}\Phi', \quad (x, z) = K(x', z'), \quad t = t'\omega, \quad \zeta = \frac{\zeta'}{A_b}, \quad h = \frac{h'}{A_b}, \tag{5.5}$$

where ω and K are related by the dispersion relation according to the linearized theory,

$$\omega^2 = gK\tanh(KH). \tag{5.6}$$

The exact dimensionless governing equations for the inviscid core are

$$\nabla^2\Phi = 0, \tag{5.7}$$

$$\zeta_t + \epsilon\Phi_x\zeta_x = \Phi_z \quad \text{on } z = KH + \epsilon\zeta, \tag{5.8}$$

$$\Phi_t + \frac{gK}{\omega^2}\zeta + \tfrac{1}{2}\epsilon|\nabla\Phi|^2 = 0 \quad \text{on } z = KH + \epsilon\zeta, \tag{5.9}$$

$$\epsilon\Phi_x h_x = \Phi_z \quad \text{on } z = \epsilon h. \tag{5.10}$$

To allow for slow modulations of the surface waves due to either narrow bandedness or Bragg resonance by a patch of bars, we introduce the following cascade of variables:

$$x,\ x_1 = \epsilon x; \qquad t,\ t_1 = \epsilon t, \quad \bar{t} = \epsilon^a t. \tag{5.11}$$

The following perturbation expansions are assumed for Φ and free surface ζ:

$$\Phi = \Phi_0(z, x, x_1, t, t_1, \bar{t}) + \epsilon\Phi_1(z, x, x_1, t, t_1, \bar{t}) + \cdots, \tag{5.12}$$

$$\zeta = \zeta_0(x, x_1, t, t_1, \bar{t}) + \epsilon\zeta_1(x, x_1, t, t_1, \bar{t}) + \cdots. \tag{5.13}$$

When (5.11)–(5.13) are substituted into (5.7)–(5.10) and the boundary conditions are expanded in Taylor series about $z = KH$ on the free surface and $z = 0$ on the bottom, the perturbation problems for the first two orders can be solved as in Mei (1985). We only cite the results below.

At leading order $O(\epsilon^0)$, the bottom is flat. The linearized solution is

$$\zeta_0 = \frac{\sinh(KH)}{2}(A\mathrm{e}^{-\mathrm{i}x} - B\mathrm{e}^{\mathrm{i}x})\mathrm{e}^{\mathrm{i}t} + \text{c.c.}, \tag{5.14}$$

$$\Phi_0 = \frac{\mathrm{i}}{2}\cosh z(A\mathrm{e}^{-\mathrm{i}x} - B\mathrm{e}^{\mathrm{i}x})\mathrm{e}^{\mathrm{i}t} + \text{c.c.}, \tag{5.15}$$

subject to the dispersion relationship (5.6). For later convenience, we shall refer to A as the incident wave and B as the reflected wave.† Note that A is the surface amplitude of the incident wave.

At the second order $O(\epsilon)$, the solution for Φ_1 is the superposition of three time harmonics $\mathrm{e}^{\pm\mathrm{i}nt}$ with $n = 0, 1, 2$, i.e.

$$\Phi_1 = \Phi_1^{[0]} + \Phi_1^{[1]} + \Phi_1^{[2]}, \tag{5.16}$$

where the superscript refers to the time harmonic. We quote the result for $\Phi_1^{[2]}$ which will be needed to determine the boundary layer flow in the next section:

$$\Phi_1^{[2]} = \frac{3\mathrm{i}}{16}\frac{\cosh 2z}{\sinh^2 KH}(A^2\mathrm{e}^{-2\mathrm{i}x} + B^2\mathrm{e}^{2\mathrm{i}x})\mathrm{e}^{2\mathrm{i}t} + \text{c.c.} \tag{5.17}$$

For the first-harmonic component, the solvability for $\Phi_1^{[1]}$ gives the evolution equations for the amplitudes A and B of the leading-order waves:

$$\frac{\partial A}{\partial t_1} + \frac{1}{2}\left(1 + \frac{2KH}{\sinh 2KH}\right)\frac{\partial A}{\partial x_1} = -\frac{\mathrm{i}D_1 B}{2\sinh 2KH}, \tag{5.18}$$

$$\frac{\partial B}{\partial t_1} - \frac{1}{2}\left(1 + \frac{2KH}{\sinh 2KH}\right)\frac{\partial B}{\partial x_1} = -\frac{\mathrm{i}D_1^* A}{2\sinh 2KH}, \tag{5.19}$$

where D_1 and its complex conjugate D_1^* are the first-harmonic amplitudes of the bar profile

$$h = \sum_{m\neq 0}^{\infty}(\tfrac{1}{2}D_m\mathrm{e}^{-2\mathrm{i}mx} + \tfrac{1}{2}D_m^*\mathrm{e}^{2\mathrm{i}mx}), \quad m \in N. \tag{5.20}$$

The two equations (5.18) and (5.19) are formally the same as those obtained by Mei (1985) for rigid bars. However, D_1 is coupled with A and B via the bar evolution equation (4.12), hence the complete problem coupling bars and waves is highly nonlinear. The absence of viscous attenuation is the result of assumption (2.4). As was seen in the last section, the spatial average over one bar length $\langle h\rangle$ is $O(\epsilon)$, hence D_0 is omitted from the series (5.20).

† In this paper the terms *incident, right-going* and *shoreward* are used interchangeably. Similarly the terms *reflected, left-going* and *seaward* are synonymous.

5.3. *Bottom boundary layer*

As usual, the momentum equations can be combined to yield the vorticity equation for the stream function ψ' defined by $u' = \psi'_{z'}$, $w' = -\psi'_{x'}$. In view of (2.3) and (2.4), the bar height is much greater than the thickness of the boundary layer. We shall introduce a boundary-conforming, non-orthogonal coordinate system (x', η') with

$$\eta' = z' - h'(x', t'). \tag{5.21}$$

Let the following normalization be chosen for the boundary layer flow:

$$x = x'K, \quad \eta = \frac{\eta'}{\delta}, \quad t = t'\omega, \quad \psi = \frac{\psi'}{A_b\omega\delta}, \quad h = \frac{h'}{A_b}. \tag{5.22}$$

The dimensionless form of the vorticity equation is

$$\nabla^2\psi_t - \epsilon\frac{\partial(\psi, \nabla^2\psi)}{\partial(x, \eta)} = \tfrac{1}{2}\nabla^2\nabla^2\psi, \tag{5.23}$$

where ∇^2 is the Laplacian in the new coordinates,

$$\nabla^2 = \left(K\delta\frac{\partial}{\partial x} - \epsilon\frac{\partial h}{\partial x}\frac{\partial}{\partial \eta}\right)^2 + \frac{\partial^2}{\partial \eta^2}. \tag{5.24}$$

The approximate conditions on the sea bottom (5.1) and (5.2) become

$$\frac{\partial\psi}{\partial x} = O(\epsilon^4) \quad \text{on } \eta = 0, \tag{5.25}$$

$$\left\{\frac{\partial\psi}{\partial\eta}\right\}^{[1]} = O(\epsilon), \quad \left\{\frac{\partial\psi}{\partial\eta}\right\}^{[0,2]} = O(\epsilon^2) \quad \text{on } \eta = 0. \tag{5.26}$$

Outside the boundary layer, ψ must join smoothly with the inviscid flow. The stream function in the inviscid core can be easily found as the harmonic conjugate of the velocity potential by the Cauchy–Riemann condition, and is omitted here for brevity.

Inside the boundary layer we assume (5.11) and the expansion

$$\psi = \psi_0(z, x, x_1, t, t_1, \bar{t}\,) + \epsilon\psi_1(z, x, x_1, t, t_1, \bar{t}\,) + \cdots. \tag{5.27}$$

From (5.23), (5.25) and (5.26), the following perturbation problems are found at the first two orders. By a straightforward analysis, the solution at leading order $O(\epsilon^0)$ is just the Stokes solution in the new plane (x, η),

$$\psi_0 = \tfrac{1}{2}\left[\eta - \frac{1-\mathrm{i}}{2}(1 - \mathrm{e}^{-(1+\mathrm{i})\eta})\right](A\mathrm{e}^{-\mathrm{i}x} + B\mathrm{e}^{\mathrm{i}x})\mathrm{e}^{\mathrm{i}t} + \text{c.c.} \tag{5.28}$$

Thus, the bed shear stress at the leading order, $\psi_{0,\eta\eta}$ at $\eta = 0$, does not depend on the bar height.

At the second order $O(\epsilon)$, the solution is the sum of the zeroth, first and second harmonics in time:

$$\psi_1 = \psi_1^{[0]} + \psi_1^{[1]} + \psi_1^{[2]}. \tag{5.29}$$

For the even harmonics $\psi_1^{[0]}$ and $\psi_1^{[2]}$, the governing equations are

$$\psi^{[n]}_{1,t\eta\eta} - \tfrac{1}{2}\psi^{[n]}_{1,\eta\eta\eta\eta} = \left\{\frac{\partial(\psi_0, \psi_{0,\eta\eta})}{\partial(x, \eta)}\right\}^{[n]}, \tag{5.30}$$

subject to the boundary condition on the bar surface

$$\psi^{[n]}_{1,\eta} = 0, \quad \psi^{[n]}_{1,x} = 0 \quad \text{on } \eta = 0, \tag{5.31}$$

where $n = 0, 2$. Since the flow in the core region is inviscid and irrotational up to $O(\epsilon^2)$, the shear stress vanishes at the outer edge of the boundary layer. As a consequence, we have a matching condition for the zeroth harmonic,

$$\psi_{1,\eta\eta}^{[0]} = 0 \quad \text{as } \eta \to \infty, \tag{5.32}$$

and for the second harmonic,

$$\psi_1^{[2]} \to \frac{3\eta}{8\sinh^2 KH}(A^2 e^{-2ix} - B^2 e^{2ix})e^{2it} + \text{c.c.} \quad \text{as } \eta \to \infty. \tag{5.33}$$

These conditions are of the same form as those for the second-order boundary layer flow over a flat bed. The solutions, when expressed in the (x, η) coordinates, are formally the same as the classical results of Longuet-Higgins (1953),

$$\psi_1^{[0]} = \left\{ \left(\tfrac{1}{4}\eta + \frac{3+5i}{8} \right) e^{-(1-i)\eta} - \frac{1-i}{8}(e^{-(1+i)\eta} + \tfrac{1}{2}e^{-2\eta}) + \frac{3+3i}{8}\eta - \frac{3+13i}{8} \right\}$$
$$\times(|A|^2 - |B|^2 + AB^* e^{-2ix} - A^* B e^{2ix}) + \text{c.c.}, \tag{5.34}$$

$$\psi_1^{[2]} = \left\{ \frac{1-i}{2\sqrt{2}} \left(\frac{3}{8\sinh^2(KH)} + \tfrac{1}{4} \right) (e^{-\sqrt{2}(1+i)\eta} - 1) + \tfrac{1}{4}\eta e^{-(1+i)\eta} + \frac{3}{8\sinh^2(KH)}\eta \right\}$$
$$\times(A^2 e^{-2ix} - B^2 e^{2ix})e^{2it} + \text{c.c.} \tag{5.35}$$

Thus, $\psi_1^{[0]}$ and $\psi_1^{[2]}$ are respectively the wave-induced steady streaming and the second-harmonic field in the boundary layer. Note that the bottom shear stresses associated with these two components, $\psi_{1,\eta\eta}^{[0]}$ and $\psi_{1,\eta\eta}^{[2]}$ on $\eta = 0$, do not depend on the bar height h.

6. Properties of the bar evolution equation

Substituting the solutions of ψ_0, $\psi_1^{[0]}$ and $\psi_1^{[2]}$ into (4.13) and (4.14), the following explicit expressions for the diffusivity and the forcing can be derived:

$$D_v = \frac{4\beta}{\pi(1-n)} \frac{Q_{s0}}{\widehat{\psi_{0,\eta\eta}}}, \tag{6.1}$$

$$-\frac{\partial q_\tau}{\partial x} = -\frac{4(\frac{1}{2} + \frac{2}{3}\mathscr{H})}{\pi(1-n)}|A|^2 \Theta_0 \frac{\partial}{\partial x}\left\{ \frac{Q_{s0}}{\widehat{\psi_{0,\eta\eta}}}(1 - |R|^2 - 2|R|\sin(2x + \theta_R)) \right\}, \tag{6.2}$$

where

$$\widehat{\psi_{0,\eta\eta}} = \sqrt{2}|A|\sqrt{1 + |R|^2 + 2|R|\cos(2x + \theta_R)}, \tag{6.3}$$

$$\mathscr{H} = \left(\frac{3}{8\sinh^2(KH)} + \tfrac{1}{4} \right)\sqrt{2} - \tfrac{1}{2}. \tag{6.4}$$

Q_{s0} is defined in (4.10), and is a function of $\widehat{\psi_{0,\eta\eta}}$ only. $R = B/A = |R|e^{i\theta_R}$ is the local complex reflection coefficient. Note that the empirical phase angle $\Delta\varphi$ disappears after the time averaging.

For finite reflection the forcing term $(-\partial q_\tau/\partial x)$ and the diffusivity in the diffusion equation (4.15) are both periodic in x with the period π, i.e. one half the surface wavelength. Thus, wave-induced bottom stress generates sand bars with spacings equal to half of the water wavelength. Through the coefficient β, gravitational force on the sediment particles leads to sediment diffusion which is also affected by the

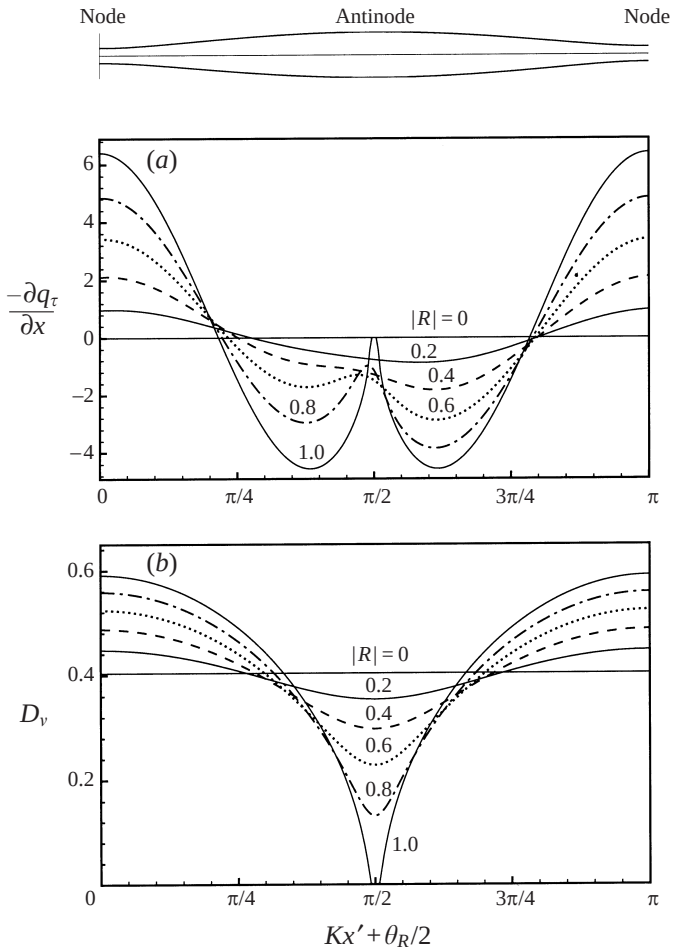

FIGURE 1. Forcing and diffusivity in half of a local wavelength. $\Theta_0 = 0.55$, $\epsilon = 0.04$, $\beta = 0.2$.

local bed stress via $Q_{s0}/\widehat{\psi_{0,\eta\eta}}$. In the limit of a purely progressive wave ($R = 0$), $\widehat{\psi_{0,\eta\eta}}$ and Q_{s0} reduce to constants. Consequently, the diffusivity D_v is uniform in x and the forcing $(-\partial q_\tau/\partial x)$ vanishes everywhere. Without reflection, sand bars cannot be formed from a flat bed. On the other hand, with any non-zero reflection, sand bars can be formed, whether or not the mean current in the boundary layer is cellular. This was first noted experimentally by O'Hare & Davies (1993).

The forcing term $(-\partial q_\tau/\partial x)$ depends on both the wave-induced steady streaming $\psi_1^{[0]}$ and the second harmonic $\psi_1^{[2]}$. This result modifies the earlier expectation (Carter *et al.* 1973) that the time-averaged mass transport corresponding to $\psi_1^{[0]}$ is solely responsible for the formation of sand bars. Clearly, the spatial variation of the sand flux q_τ caused by the wave stresses leads to periodic erosion and deposition on an initially flat bed.

We now present some sample numerical values of $(-\partial q_\tau/\partial x)$ and D_v. The wave and sediment parameters are: wave period $T = 8$ s, water depth $H = 7$ m, local incident wave amplitude $A_0 = 25$ cm and sand diameter $d = 0.4$ mm. By the empirical procedure in Appendix A, the estimated ripple height is 6.57 cm, wave friction factor 0.148 and eddy viscosity $\nu = 4.79\,\mathrm{cm^2\,s^{-1}}$. From the Shields diagram, $\Theta_c = 0.035$.

Using these inputs, we get: $\epsilon = 0.0328$, $\Theta_0 = 0.55$ and the slow time $\bar{t} = \epsilon^a \omega t' = 2.50 \times 10^{-6} \omega t'$ with $C_s = 3$. The slope factor is chosen to be $\beta = 0.2$, which is within the empirical range for fitting the experiments to be discussed in § 9. The ratio $\Theta_0/\Theta_c = 15.8$ is fairly large. In figure 1, the forcing and diffusivity are plotted as functions of x for various reflection coefficients. Because of the spatial periodicity, only half of the surface wavelength between two adjacent minima (or nodes) of the surface envelope is plotted.

As shown in figure 1(*a*), the forcing term $(-\partial q_\tau/\partial x)$ is in general non-zero except for zero reflection, and asymmetric with respect to a wave antinode (envelope maximum), except for $|R| = 1$. Under a wave node where the horizontal orbital velocity is greatest near the bed, the forcing is positive for all finite $|R|$, hence causing deposition of sand and form a bar crest. Under a wave antinode where the horizontal orbital velocity is the smallest, the forcing is negative, hence causing erosion and form a bar trough. For a partially reflected wave $0 < |R| < 1$, the strongest erosion occurs downwave of the wave antinode.† For near perfect reflection, erosion is zero directly beneath the antinode and attains maxima on both sides of the antinode.

For a given $|R|$, $D_v(x)$ in figure 1(*b*) is symmetrical in x with respect to a wave antinode. The maximum of D_v occurs at a node and the minimum at an antinode. This is attributable to the fact that the tangential velocity above, and the shear stress on, the bed is largest under a wave node (near a bar crest) and smallest under an antinode (near a bar trough). Thus gravity counteracts the forcing due to the bed shear and tends to limit the growth of bars. In principle, an equilibrium state can be achieved when the total transport rate becomes uniform within a bar wavelength.

When local reflection is strong, e.g. $|R| = 1$, the bottom shear stress under a wave antinode is too weak to move any sand; both diffusivity and forcing are zero there, see figure 1. Within a small neighbourhood of the antinode, the bed surface should remain unchanged. Note that the bar slopes at both ends of this sub-critical region can be theoretically steep because of the discontinuity of $\partial^2 q_\tau/\partial x^2$ and $\partial^2 D_v/\partial x^2$. This local discontinuity is an inherent defect of the simple sediment transport model valid only for small $\partial h/\partial x$. In reality, local avalanches may occur to reduce the bed slope to at most the angle of repose. A better model must allow for finite slope of the bar surface.

The parameter $\mathscr{H}$ appearing in the forcing term decreases exponentially with increasing KH, to $\sqrt{2}/4 - \frac{1}{2} = -0.15$ in deep water. It becomes unbounded when $KH \to 0$, as $(KH)^{-2}$, signifying the need for a nonlinear shallow water theory.

7. The steady state

While the evolutions of bars and waves are coupled in general, and will be examined later, partial insight can be gained from the analytical results for the steady state in terms of the local wave intensity. We caution however that the steady state is an idealization since waves in nature can vary in time long before the steady state is reached, due to the change of wind and/or to wave–wave interactions inherent in the nonlinearity on the free surface.

In this section, the wave amplitudes A and B are taken as known constants. At the steady state, diffusion by gravity balances the transport by wave stresses, so that the total sediment transport rate is constant within a bar wavelength. Omitting the time derivative, we integrate (4.12) with respect to x once, and use (6.1) and (6.2) to get

† Downwave is the direction of incident wave propagation.

the bar slope,

$$\frac{4\beta}{\pi(1-n)}\frac{Q_{s0}}{\widehat{\psi_{0,\eta\eta}}}\frac{\partial h_S}{\partial x}=\frac{4\Theta_0}{\pi(1-n)}(\tfrac{1}{2}+\tfrac{2}{3}\mathscr{H})|A|^2\frac{Q_{s0}}{\widehat{\psi_{0,\eta\eta}}}(1-|R|^2-2|R|\sin(2x+\theta_R))-q_e, \tag{7.1}$$

where q_e is an as yet unknown constant of integration and represents the net transport rate at the steady state. The constants of integration are determined by requiring the periodicity of h_S, i.e. $h_S(\pi)=h_S(0)$, and local mass conservation,

$$\int_0^\pi h_S\,\mathrm{d}x=0. \tag{7.2}$$

The threshold condition in (4.10) implies $Q_{s0}=0$ when

$$\sqrt{1+|R|^2+2|R|\cos(2x+\theta_R)}>\frac{1}{\sqrt{2}|A|}\frac{\Theta_c}{\Theta_0}\equiv\widehat{\Theta}_c. \tag{7.3}$$

Since the minimum of the left-hand-side is $(1-|R|)$, which occurs when $\cos(2x+\theta_R)=-1$, the flow is supercritical for all x if $|R|<1-\widehat{\Theta}_c$. Otherwise sand particles remain immobile over part of the bed. We now distinguish two cases.

Weak reflection: $|R|<1-\widehat{\Theta}_c$ Here the amplitude of the bottom shear stress exceeds the threshold everywhere within a bar wavelength. From (4.10), $Q_{s0}\neq 0$ for all x. Solving (7.1)–(7.2), we get the steady bar profile,

$$h_S=\frac{\Theta_0}{\beta}(\tfrac{1}{2}+\tfrac{2}{3}\mathscr{H})|A|^2(|R|\cos 2\chi+\Gamma), \tag{7.4}$$

where $\chi=x+\theta_R/2$ and

$$\Gamma=(1-|R|^2)\left\{\chi-\pi\frac{\displaystyle\int_0^\chi\frac{\widehat{\psi_{0,\eta\eta}}\,\mathrm{d}\chi}{(\widehat{\psi_{0,\eta\eta}}-\Theta_c/\Theta_0)^{1.5}}}{\displaystyle\int_0^\pi\frac{\widehat{\psi_{0,\eta\eta}}\,\mathrm{d}\chi}{(\widehat{\psi_{0,\eta\eta}}-\Theta_c/\Theta_0)^{1.5}}}\right\}. \tag{7.5}$$

The transport rate at steady state is

$$q_e=\frac{4\Theta_0}{1-n}(\tfrac{1}{2}+\tfrac{2}{3}\mathscr{H})\frac{|A|^2(1-|R|^2)}{\displaystyle\int_0^\pi\frac{\widehat{\psi_{0,\eta\eta}}\,\mathrm{d}\chi}{(\widehat{\psi_{0,\eta\eta}}-\Theta_c/\Theta_0)^{1.5}}}. \tag{7.6}$$

Thus, as reflection increases, the net sediment transport decreases.

Strong reflection: $|R|>1-\widehat{\Theta}_c$ Here the reflection is so strong that the amplitude of the bottom shear stress in a small stretch beneath the surface antinode is below the threshold, hence no sediment motion occurs there. It follows that $q_e\equiv 0$ everywhere.

Given a reflection $|R|$, the flow is sub-critical in $\chi_c\leqslant\chi\leqslant\pi-\chi_c$, where $\chi_c<\pi/2$ and satisfies

$$\sqrt{1+|R|^2+2|R|\cos(2\chi_c)}=\widehat{\Theta}_c. \tag{7.7}$$

Inside this region, we assume that there is no wave activity at all earlier times, so $h_S=0$. Outside this region, $\chi<\chi_c$ or $\chi>\pi-\chi_c$, $Q_{s0}\neq 0$ and (7.1) is still valid with

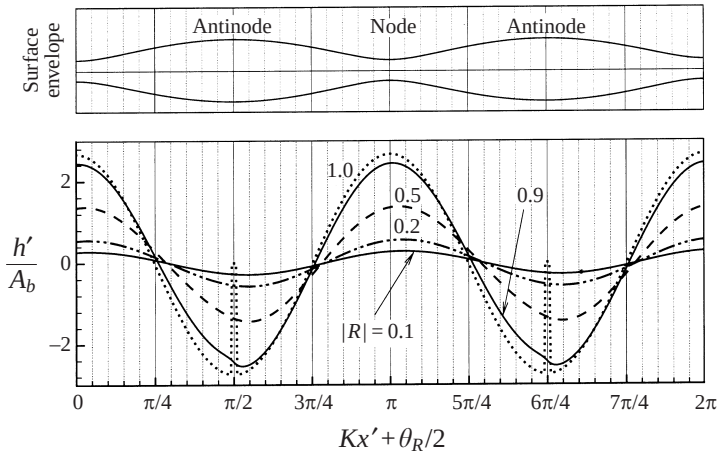

FIGURE 2. Steady bar profiles in one local wavelength.

$q_e = 0$. The solution is found to be

$$h_S = \frac{\Theta_0}{\beta}(\tfrac{1}{2} + \tfrac{2}{3}\mathscr{H})|A|^2(|R|\cos 2\chi + \Gamma), \tag{7.8}$$

where

$$\Gamma = \begin{cases} (1-|R|^2)\chi - \dfrac{|R|\sin 2\chi_c}{2\chi_c} & \text{if } \chi < \chi_c \\ -|R|\cos 2\chi & \text{if } \chi_c < \chi < \pi - \chi_c \\ (1-|R|^2)(\chi-\pi) - \dfrac{|R|\sin 2\chi_c}{2\chi_c} & \text{if } \pi - \chi_c < \chi < \pi. \end{cases} \tag{7.9}$$

By invoking periodicity of h_S and local mass conservation, h_S becomes discontinuous at $\chi = \chi_c$ and $\chi = \pi - \chi_c$. Local avalanches should occur to modify the predictions here. As shown in an earlier example, figure 1, the ratio Θ_c/Θ_0 is small for quite ordinary waves. The poor prediction is therefore limited to a very small range for $|R| \simeq 1$. For stronger waves, Θ_0 is greater and this range of poor prediction is smaller.

As will become clear later, after accounting for the coupled evolution of waves and bars, the site of the sub-critical region changes during the course of evolution. A region which is sub-critical at one stage may be partially (or completely) eroded later. In other words, the profile of h_S in the sub-critical region is not necessarily zero and depends on the history of the evolution. Nevertheless, there can be portions of the seabed where the sub-critical region changes very little throughout the evolution. The steady-state solution given here is in principle possible.

Figure 2 shows the steady bar profiles for various reflection coefficients, while the incident wave and sand properties are the same as those for figure 1. The bar crest is located slightly downwave of the local wave node for small reflection, see $|R| = 0.1, 0.2, 0.5$, and directly beneath the node when $|R| = 1$. The bar height (crest to trough) increases with $|R|$. The sub-critical region first occurs when $|R| = 0.955$, at which the bar profile is discontinuous near the trough. As $|R|$ further increases, a thin peak emerges across the discontinuity, with the troughs on both sides approaching the same depth. For $|R| = 1$, the dimensionless width of this peak is only 0.045, about 1.4% of the total bar length. Thus the range of $|R|$ for which the theory is invalid is of minor practical consequence.

We now examine the bar evolution by accounting for the possible interaction between bars and waves through Bragg scattering.

8. Numerical procedure for coupled evolution

Because the time scale of the bar evolution is much longer than that of Bragg scattering, the wave response over the sand bed is quasi-steady. Therefore, $\partial/\partial t_1 = 0$ in the wave envelope equations (5.18) and (5.19).

For explaining the computational procedure we take the case where the bed is erodible only within $0 < x_1 < \ell$ and rigid elsewhere. At $x_1 = 0$, $A(0, \bar{t}) = A_I$ is given by the known amplitude of the incoming waves. At $x_1 = \ell$ the complex reflection coefficient is specified based on the location and condition of the shoreline, i.e. $B(\ell, \bar{t})/A(\ell, \bar{t}) = R_\ell \equiv |R_\ell| e^{i\theta_{R_\ell}}$. For given A and B, h is solved from (4.15) for a period of π in the short scale x. D_1 is then computed from the Fourier expansion of h. For an initially flat bed, we must have $D_1(x_1, 0) = 0$.

At each time step $\bar{t}_n$, numerical Fourier decomposition is performed for the computed h to get D_1 at each grid point of x_1. Equations (5.18) and (5.19) are then solved for the long scale variations of A and B by the fourth-order Runge–Kutta method, subject to the boundary conditions at $x_1 = 0$ and ℓ. By using these wave solutions, (4.15) is solved by a finite difference method to obtain h at the next time $\bar{t}_{n+1}$, with x_1 as a parameter. Periodicity boundary conditions are imposed. A scheme of forward difference in time and central difference in space is employed. Once h is found for all x_1, A and B at time $\bar{t}_{n+1}$ are solved by the same procedure as at $\bar{t}_n$.

9. Comparison with experiments

A test of the present theory is made by numerical simulation of the laboratory observations of Herbich *et al.* (1965) who performed experiments in a wave tank 20.6 m long, and 61 cm wide and deep. A flap-type wavemaker was installed at one end and a seawall at the other. Measured from the horizontal bottom, the inclination of the seawall was set to be 15°, 30°, 45°, 67.5° and 90°. A layer of sand, 12.7 cm thick, was placed on the bottom of the tank for a distance of 11.28 m in front of the seawall. Before each test the sand was levelled. A false bottom was mounted under and in front of the wavemaker to the edge of the sandy bed so that the entire bed was flat initially. For the purpose of visualization, the sand was well washed before the test to eliminate the suspensions of fine particles. The mean diameter of the sand on the bed was $d = 0.48$ mm.

We shall focus on the data for three tests with steep seawalls (45°, 67.5° and 90°) from which the beach reflection was essentially perfect, i.e. $|R_\ell| \simeq 1.0$. The wall inclination only affects the phase of the reflection coefficient. The wave conditions in these three tests are listed in table 1. The standing wave height (crest to trough) measured in the experiment is taken to be equal to $4A_0$.

Half-wavelength sand bars, with ripples superimposed on them, were found to form along the bed. Only the spatially averaged depth of scour, measured from the mean bed position to each bar trough, was reported as a function of time. No detailed records of the ripple height were reported by Herbich *et al.*, except that the maximum was approximately 2 cm. We have used the empirical method in Appendix A to estimate the ripple height, under the experimental conditions, in order to estimate the eddy viscosity. Based on the information in table 1, the input parameters for numerical simulations are obtained and given in table 2. The value $C_s = 1.95$ of

	Test 1	Test 2	Test 3
Wave amplitude A_0 (cm)	1.56	2.05	2.36
Wave period T (s)	1.50	1.50	2.00
Water depth H (cm)	12.7	17.15	21.29
Wavelength $2\pi/K$ (cm)	161.54	185.93	269.24
KH	0.495	0.582	0.495
$A_b = A_0/\sinh(KH)$ (cm)	3.39	3.33	4.58

TABLE 1. The incident wave conditions in tests 1, 2, 3 (Herbich *et al.* 1965).

	Test 1	Test 2	Test 3
Average ripple height (cm)	0.81	0.80	1.09
Maximum ripple height under the wave node (cm)	1.39	1.37	1.85
Wave friction factor f_w	0.160	0.162	0.154
Eddy viscosity ν (cm^2 s^{-}1)	0.308	0.300	0.405
$\epsilon = A_b K$	0.132	0.113	0.107
Θ_0	0.146	0.141	0.147
α	164.6	186.1	278.1
$\epsilon\Theta_0^{1/2}/\alpha = \epsilon^a$	3.08×10^{-4}	2.27×10^{-4}	1.47×10^{-4}

TABLE 2. The input parameters for numerical simulation.

Sleath (1982) is used in calculating α. Note that the ripples are the highest under a wave node where the orbital amplitude of wave oscillation is $2A_b$.

Using the parameters in table 2, we compute the evolution of bars and waves under the experimental conditions. For each test, β is so adjusted that the predicted bar heights at late stages (i.e. close to steady state) agree with the data. Figure 3 shows the comparison of the averaged depth of the bar troughs during the course of the evolution. The depth is normalized by the surface wave height $4A_0$ as in the original data. It has been pointed out in § 6 that for $|R| = 1$ the computed profile has unrealistically sharp peaks at the bar troughs beneath the wave antinodes. Except for these peaks, the predicted bar profiles are nearly sinusoidal, as can be seen in figure 4 for test 3 with 90° seawall. For comparision we also plot the height of the bar crests, after averaging over the entire bar patch. The time evolution and spatial variations of the bar height, also normalized by $4A_0$, together with the incident wave amplitude $|A|$, are shown in figure 5 at different times for test 3.

The data for tests 1 and 3, representing the measured depths of the bar troughs for three different wall inclinations 45°, 67.5° and 90°, fall nearly onto a single curve, suggesting that the phase of the beach reflection θ_{R_r} is not important to the bar height. With a minor adjustment of β within a reasonable range, close to the value used by Fredsøe for river bars, the agreement between the predictions and the data is fairly good during the transient evolution. The predicted initial growth is, in general, slightly higher than the data. In view of the inaccuracy associated with the empirical formulae for the transport rate, bottom roughness for a rippled bed and the eddy viscosity, the general agreement in the initial growth is still encouraging. No records of the position of the bar crests and troughs have been reported by Herbich *et al.*, aside from a comment that 'The most that can be said is that at any time there will always be scouring within a distance of at least $\frac{1}{4}$ L(water wavelength) or less from

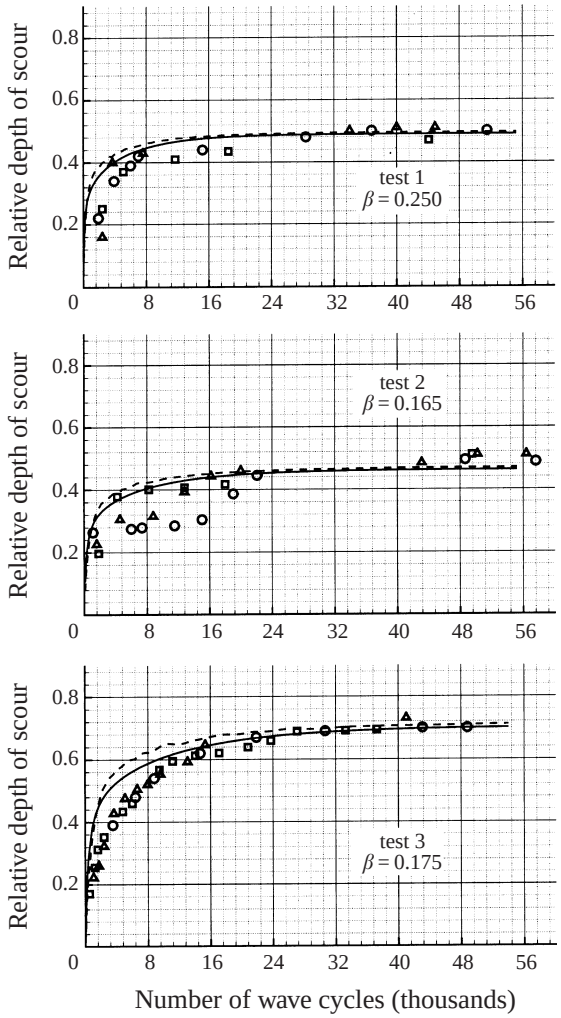

FIGURE 3. The averaged depth of bar trough (normalized by the surface wave height) as a function of time. Solid curve: the predicted height of bar crest above the mean bed position. Dashed curve: the predicted depth of bar trough below the mean bed position. Data (symbols) are from Herbich *et al.* (1965).

the face of the wall'. This comment is not inconsistent with our theory, according to which a bar trough must be next to the wall (see figure 4).

Similar laboratory experiments have been reported by Boczar-Karakiewicz *et al.* (1981), whose primary interest is the formation of very long sand bars of length comparable with the recurrence length associated with the nonlinear harmonic generation in shallow water. In one of their tests with a vertical wall at the end of the flume, only the half-water-wavelength sand bars were formed. From the few snapshots (19, 26, and 34 hours after the start) reported, it is evident that the bar crests are beneath the wave envelope nodes (see figure 6 of their paper). Since no data for the evolving stages are available and all reported records correspond to the steady state, no meaningful quantitative comparison can be made with our theory here.

We shall now study two theoretical examples in detail in order to understand the mutual influence of waves and bars. In each example, an analytical discussion of

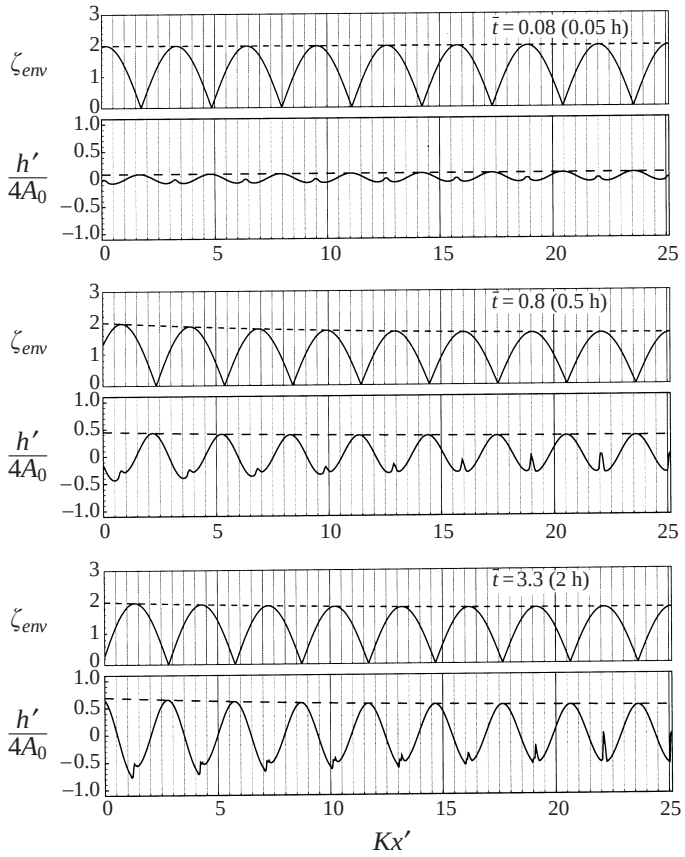

FIGURE 4. The surface envelope and bar profile at early stages under the experimental conditions of test 3 in Herbich *et al.* (1965).

the wave envelope equations is given first, followed by numerical results for input parameters common in the field.

10. Waves over a finite stretch of erodible bed

Consider a monchromatic wavetrain incident from $x' \sim -\infty$ and passing over an initially horizontal bed which is semi-infinite in extent. The bed is erodible in $0 < x' < L$, and non-erodible elsewhere. At $x' = L$, the reflection coefficient is given.

10.1. *Qualitative analysis*

Let us denote the local complex reflection coefficient by

$$R(\bar{t}, x_1) \equiv |R|e^{i\theta_R} = B/A. \tag{10.1}$$

Defining $A \equiv t|A|e^{i\theta_A}$, we then get the polar form of (5.18) and (5.19), with $\partial/\partial t_1 = 0$ at the steady state, as follows:

$$C_g \frac{\partial |A|}{\partial x_1} = \frac{|R||A|}{2 \sinh 2KH} \widehat{D}_1^i, \tag{10.2}$$

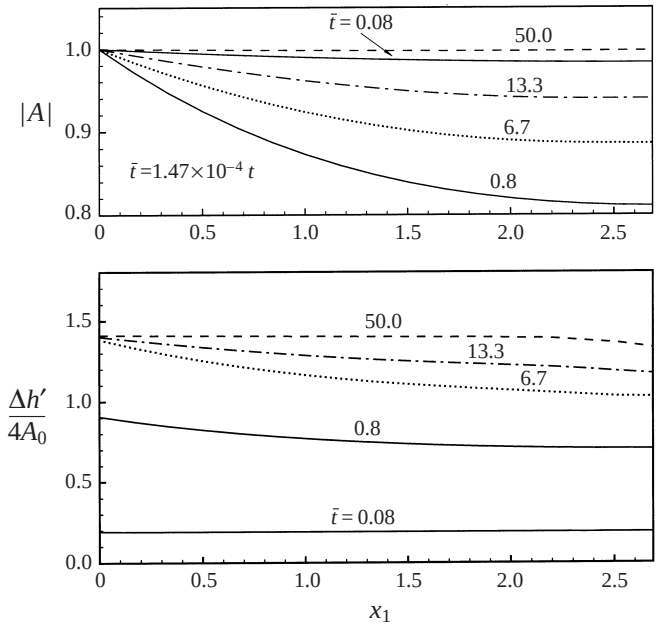

FIGURE 5. Slow variations of the incident wave amplitude and the bar height under the experimental conditions of test 3 in Herbich *et al.* (1965).

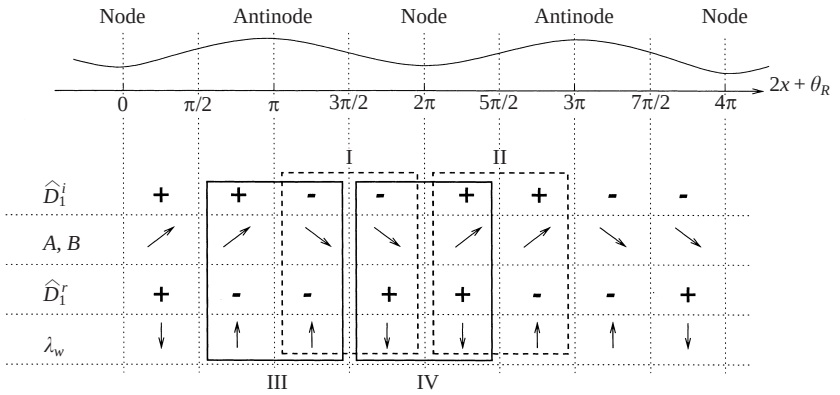

FIGURE 6. Position of bar crests relative to wave envelope nodes (antinodes).

$$C_g \frac{\partial \theta_A}{\partial x_1} = -\frac{|R|}{2 \sinh 2KH} \widehat{D}_1^r, \tag{10.3}$$

$$C_g \frac{\partial |R|}{\partial x_1} = \frac{1 - |R|^2}{2 \sinh 2KH} \widehat{D}_1^i, \tag{10.4}$$

$$C_g \frac{\partial \theta_R}{\partial x_1} = \frac{1 + |R|^2}{|R| 2 \sinh 2KH} \widehat{D}_1^r, \tag{10.5}$$

where the superscripts r and i stand for the real and imaginary parts of the complex coefficient $\widehat{D}_1$, defined as

$$\widehat{D}_1 = D_1 e^{i\theta_R}. \tag{10.6}$$

The boundary conditions are

$$|A(0,\bar{t})| = 1, \quad \theta_A(0,\bar{t}) = 0 \quad \text{at } x_1 = 0, \tag{10.7}$$

and

$$|R(\ell,\bar{t})| = |R_\ell|, \quad \theta_R(\ell,\bar{t}) = \theta_{R_\ell} \quad \text{at } x_1 = \ell \equiv \epsilon K L. \tag{10.8}$$

It is easy to show from (5.18) and (5.19) that the conservation of total energy flux at the steady state, i.e. $|A(x_1,\bar{t})|^2 - |B(x_1,\bar{t})|^2$, is constant in x_1. From (10.2) the energy flux of the incident waves is given by

$$C_g \frac{\partial}{\partial x_1}(\tfrac{1}{2}|A|^2) = \frac{|A||B|}{2\sinh 2KH}\widehat{D}_1^i. \tag{10.9}$$

Consequently

$$-C_g \frac{\partial}{\partial x_1}(\tfrac{1}{2}|B|^2) = -\frac{|A||B|}{2\sinh 2KH}\widehat{D}_1^i. \tag{10.10}$$

The negative sign on the left of (10.10) is kept to emphasize that the energy of B is transported seaward ($-x$). Thus, if $\widehat{D}_1^i$ is positive at a point x_1, local Bragg scattering causes energy to be transferred from B to A. At any x_1, A is increased to the right by gaining energy from B, and B is reduced to the left, i.e. both A and B increase locally in the positive x_1-direction (shoreward). On the other hand, if $\widehat{D}_1^i$ is negative, local energy transfer is from A to B. Thus, A decreases shoreward and B increases seaward, or equivalently, A and B both decrease shoreward. In the meantime, it is seen from (10.3) that the sign of $\widehat{D}_1^r$ determines how the local wavelength of the waves is affected. For the velocity potential given in (5.15), the local phase of the incident waves is $\theta_{inc} = x - \theta_A - \omega t$. The local wavenumber of the incident waves is then

$$K_{local} = \frac{\partial \theta_{inc}}{\partial x} = 1 - \epsilon \frac{\partial \theta_A}{\partial x_1}. \tag{10.11}$$

From (10.3), $\partial\theta_A/\partial x_1$ is negative if $\widehat{D}_1^r$ is positive; hence the local wavelength of the incident waves tends to be shortened by $O(\epsilon)$. The opposite is true if $\widehat{D}_1^r$ is negative. Over the bar patch the accumulated effect of this shortening or lengthening is to change the number of bars in the patch ($0 < x_1 < \ell$).

The envelope (upper half) of the free surface (5.14) is

$$\zeta_{env} = \sqrt{|A|^2 + |B|^2 - 2|A||B|\cos(2x + \theta_R)}, \tag{10.12}$$

where $\zeta_{env} = \zeta'_{env}/A_0$. Clearly, the wave nodes (minimum vertical displacement on the free surface) occur at

$$2x + \theta_R = 0, 2\pi, 4\pi, \ldots \tag{10.13}$$

and the wave antinodes (maximum vertical displacement on the free surface) at

$$2x + \theta_R = \pi, 3\pi, 5\pi, \ldots \ . \tag{10.14}$$

The profile of sand bars is dominated by the second-harmonic terms e^{-2ix} and e^{2ix} with the amplitudes $D_1 \equiv \widehat{D}_1 e^{-i\theta_R} = |\widehat{D}_1|\exp(-i\theta_R + i\theta_D)$ and D_1^* respectively, where θ_D is the phase angle of $\widehat{D}_1$. Accordingly, the bar crests are located at

$$2x + \theta_R = 0 + \theta_D, \quad 2\pi + \theta_D, \quad 4\pi + \theta_D \ldots \ . \tag{10.15}$$

It is then obvious that the phase angle θ_D, or equivalently, the signs of $\widehat{D}_1^r$ and $\widehat{D}_1^i$, gives the position of the bar crest relative to the wave node (or antinode). With the

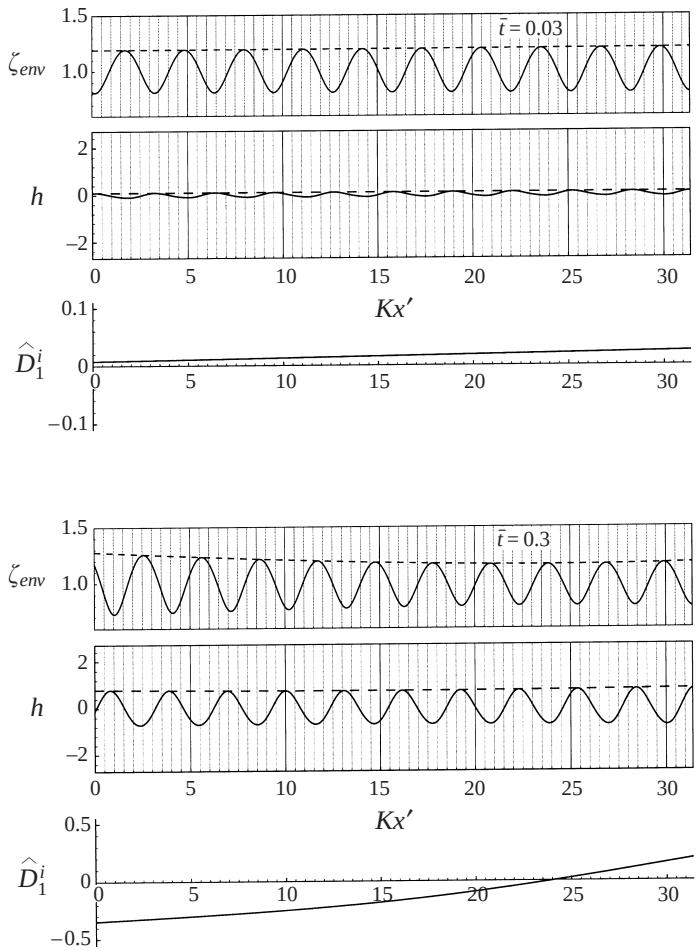

FIGURE 7. For caption see facing page.

help of figure 6, the physical implication of these phase relations can be summarized as follows.

Local wave amplitude. If a bar crest is somewhere downwave of a node of the wave envelope but upwave of the next antinode (box II), $\widehat{D}_1^i > 0$. Bragg scattering causes an energy transfer from B to A. Locally A increases shoreward and B decreases seaward (i.e. B increases shoreward too). However, if a bar crest is formed downwave of an antinode but upwave of the next node (box I), $\widehat{D}_1^i < 0$ and local energy transfer is from A to B. Both A and B decrease shoreward. No energy transfer occurs locally if a bar crest is directly beneath a wave node or antinode because $\widehat{D}_1^i = 0$. That the relative position of the bar crests and the envelope nodes affects the wave response over the bar patch was first noted in the laboratory by O'Hare & Davies (1993) and explained by Yu & Mei (2000).

Local surface wavelength. Also seen in figure 6, if a bar crest is in the neighbourhood of a node (box IV), $\widehat{D}_1^r > 0$. Bragg scattering tends to shorten the local wavelength of the waves. On the other hand, if the crest is in the neighbourhood of an antinode (box III), $\widehat{D}_1^r < 0$ and the local surface wavelength tends to increase.

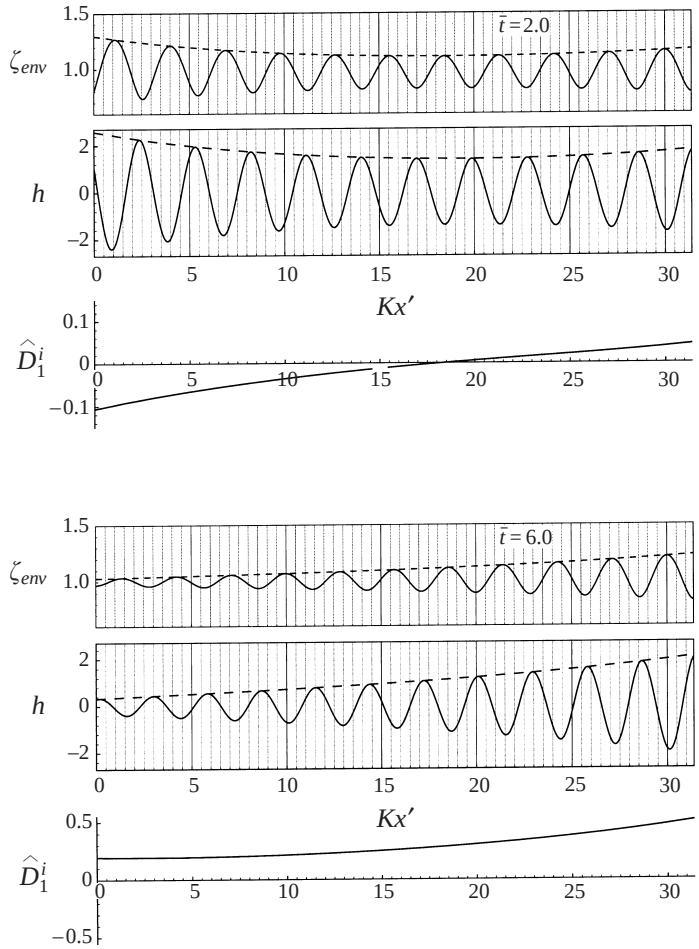

FIGURE 7. The evolution of surface envelope, bar profile and $\hat{D}_1^i$. Shore reflection is $R_\ell = 0.2$. The length of the patch is five times the incident wavelength.

In the next subsection we shall see that box IV is particularly relevant to the bars formed.

10.2. *Numerical results*

For this illustration a stronger incident wave is chosen at $x_1 = 0$: period $T = 8\,\mathrm{s}$ and amplitude $A_0 = 50\,\mathrm{cm}$ in water depth $H = 7\,\mathrm{m}$. Again, the sand diameter is $d = 0.4\,\mathrm{mm}$. For these inputs, $\nu = 15.36\,\mathrm{cm^2\,s^{-1}}$ (Appendix A) and the dimensionless parameters are: $\epsilon = 0.066$, $\Theta_0 = 1.98$ and $\bar{t} = \epsilon^a t'\omega = 4.74 \times 10^{-6} t'\omega$. Thus, $\bar{t} = 1.0$ corresponds to 3.11 days. The bed slope factor is chosen to be $\beta = 0.2$.

The length of the erodible patch is five times the wavelength of the incoming waves. At the shoreward end $x_1 = \ell$, reflection coefficient $R_\ell = 0.2$ is specified. In figure 7 the surface envelope, bar profile and $\widehat{D}_1^i$ are shown for a series of times. The sign of $\widehat{D}_1^i$ indicates on which side of the wave node the bar crest is located. Since the bar crests are beneath the nodes, $\widehat{D}_1^r$ is positive, cf. figure 6 box IV, and does not change sign during the evolution. Also, in figure 8 the incident wave amplitude $|A|$, the local reflection coefficient $|R|$ and the bar height Δh (crest to trough) are plotted against the slow scale x_1. Note that $h = h'/A_b$ where $A_b = 64.18\,\mathrm{cm}$ in this example.

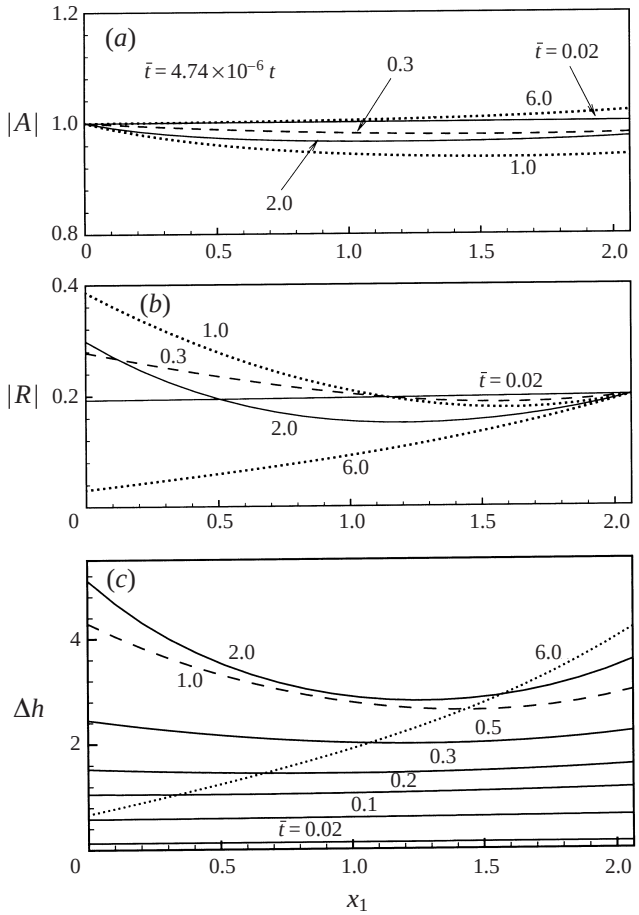

FIGURE 8. Slow variations of the incident amplitude, the local reflection coefficient and the bar height at different times. Shore reflection is $R_\ell = 0.2$. The length of the patch is five times the incident wavelength.

In the analysis in § 6 we anticipated that, without considering Bragg scattering, the bar troughs are located slightly downwave of the wave antinodes. This is seen during the early development, see figure 7 at $\bar{t} = 0.03$, when the bars are too small to have any significant effect on the waves. Every bar crest is now located slightly downwave of a wave node, since $\widehat{D}_1^r$ is positive over the entire bar patch. In accordance with figure 6, the major effect of the bars is to shorten the local wavelength of the waves. Since the phase of ζ_{env} at the shoreward end ($x_1 = \ell$) is fixed by the boundary condition (10.8), the wave nodes appear to move shoreward as a result of shortening, i.e. the wave envelope is compressed against the end $x_1 = \ell$, like a spring. This is clearly seen by comparing the number of wave crests at $\bar{t} = 0.3$ with that at $\bar{t} = 0.03$. During the early stage, the bars grow with quite uniform height across the patch, see figure 8(*c*) for $\bar{t} \leqslant 0.3$. In the meantime, Bragg scattering continues to shorten the local surface wavelength. As the nodes are compressed towards the shore, the bar crests are pulled shoreward too since the waves always tend to form bars at half-wavelength and with the crests downwave of the wave nodes. However, the shoreward migration of the bar crests is slower than that of the nodes. Over the patch, the accumulated effect of the shoreward migration of the wave nodes causes the bar crests away from the

shoreward end to lag behind the nodes, see e.g. the first four crests at the seaward end at $\bar{t} = 0.3$ in figure 7. This is also confirmed by the negative values of $\widehat{D}_1^i$ for $Kx' < 23.5$ at $\bar{t} = 0.3$. Being upwave of the nodes, these bar crests cause the local wave amplitude to decrease shoreward (see the overlap of boxes I and IV in figure 6).

As time proceeds, more crests are left behind the wave nodes, leading to a noticeable shoreward attenuation of the waves, see $\bar{t} = 1.0$ in figures 8(*a*) and 8(*b*). During this period, the reflection coefficient at the seaward end $x_1 = 0$ is increased to about 0.4, twice the value before the bars are formed. The bars are now growing at a reduced rate, see figure 8(*c*). Across the patch, the bars are significantly higher at the seaward end due to the shoreward attenuation of the wave energy. Over a longer time, the surface waves shift the bar crests shoreward so that the latter are spaced to match half the local surface wavelength. Now the region where $\widehat{D}_1^i > 0$ is increasing, see $\bar{t} = 2.0$ in figure 7, indicating that more bar crests are located downwave of the wave nodes. Close to the end at $Kx' = 31.4$, the wave amplitudes increase shoreward more noticeably. Also seen in figure 8(*a*), $\bar{t} = 2.0$, the overall shoreward attenuation of the waves becomes weaker.

Much later at $\bar{t} = 6.0$, equilibrium is almost reached; every bar crest is located slightly downwave of a wave node again, as evidenced by $\widehat{D}_1^i > 0$ everywhere. This is consistent with the steady-state results in § 7. Across the patch, the wave amplitudes increase shoreward. Accompanying such a spatial distribution of the wave energy, the bar height increases shoreward across the patch. Note that $\bar{t} = 6.0$ corresponds to a physical time of about 18.7 days. During such a long time, changes in the incident wave climate and nonlinear effects on the surface are bound to intervene.

It should be pointed out that θ_{R_ℓ}, the phase of R_ℓ, has no effect on the slow variations of waves and bars, and has been taken to be zero in the preceding computations. Changing the value of θ_{R_ℓ} will cause the locations of the nodes (and antinodes) of the wave envelope to change. As was shown in figure 1, the locations of the maximum deposition and erosion are fixed relative to the local wave nodes and antinodes. Therefore, the positions of the bar crests (and troughs) relative to the wave nodes (and antinodes) are not affected by a change of θ_{R_ℓ}; hence the variations of the local wave amplitudes and the bar height are not altered. This is in sharp contrast to the case of rigid bars, in which the phases of the wave envelope and the bars are not correlated so that the phase difference between the bars and the shore reflection R_ℓ is relevant to the wave response over the patch (Yu & Mei 2000).

We have also studied numerically a stronger shore reflection $R_\ell = 0.5$ at $x_1 = \ell$. The qualitative features of the solutions are similar to those for $R_\ell = 0.2$, except that Bragg scattering is much stronger because bars are higher. During the transient stages, the incident wave amplitude $|A|$ can be as low as 0.8 at $x_1 = \ell$, i.e. only about 64% of the incident wave energy can reach the shore. By doubling the length of the patch to ten times the incident wavelength, still with $R_\ell = 0.2$ and the same incoming wave conditions, the Bragg scattering effect is also much more pronounced. Specifically, the reflection coefficient at the seaward end can be increased to about 0.7 during the early stages. There is no equilibrium state because the computed bar height reaches the water depth in finite time.

11. Sandy bed evolution with pre-existing bars

We next consider a seabed which is erodible everywhere, $-\infty < x' < \infty$. Left from a previous storm or by artificial construction, a patch of sand bars is initially present

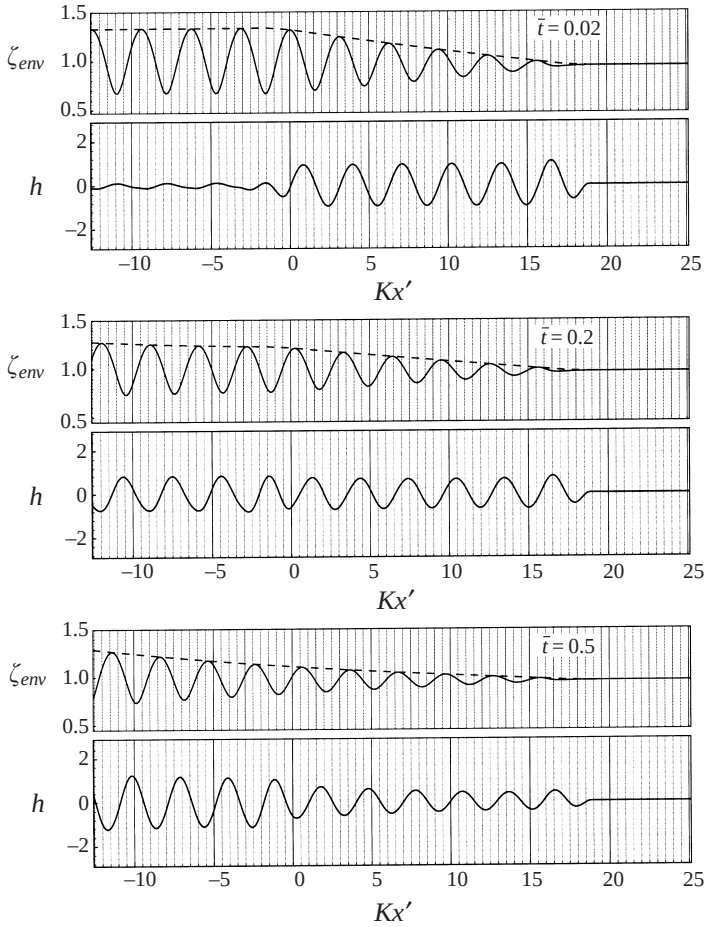

FIGURE 9. For caption see facing page.

and occupies the region $0 < x' < L$; elsewhere ($x' < 0, x' > L$) the seabed is flat. From $t_1 = 0$ onward an incident wavetrain, with wavelength twice that of the bars, arrives from $x' \sim -\infty$. At $x' = L$, $B' = 0$. Therefore, the reflected waves are only present over the bar patch and to the left, due to Bragg scattering. New offshore bars will be initiated on the incident side of the patch ($x' < 0$). However, inside the patch the wave nodes occur at $Kx' = \pi/4, 5\pi/4, \ldots$, and antinodes at $Kx' = 3\pi/4, 7\pi/4, \ldots$, as shown by Mei (1985, equations (2.13), (3.20) and (3.21)), while the bar crests are located at $Kx' = 0, \pi, \ldots$ (see equation (2.21) in Mei 1985). Clearly, each of the bar crests is upwave of a wave node by $\pi/4$ and downwave of the next antinode by $\pi/4$. Consequently, the Bragg scattered waves deposit sand into the initial bar troughs and erode the initial bar crests, cf. figure 1. While the pre-existing bars are flattened by their own scattered waves, the growth of the new offshore bars is reduced by receiving less Bragg reflection. When the old bars are nearly flattened and provide little Bragg reflection offshore, the new ones begin to be flattened similarly. Eventually all bars are wiped out. Thus, in the absence of sustained reflection from the shore, pre-existing bars cannot be maintained, and the formation of new sand bars on the sea side by Bragg reflection is at best a transient phenomenon.

In figure 9, these qualitative expectations are confirmed by a numerical example. The incident wave characteristics and sand are the same as those in § 10. Initially, six

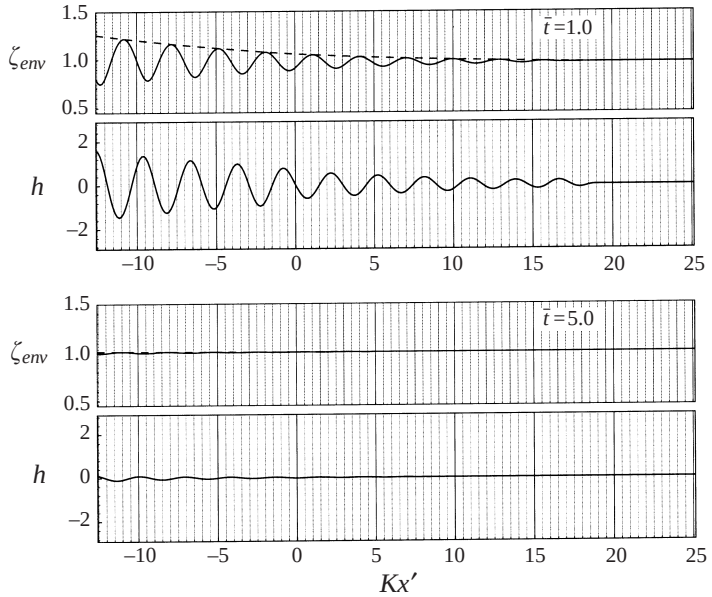

FIGURE 9. The evolution of a patch of pre-existing bars in the absence of shore reflection.

sinusoidal sand bars occupy the region $0 < Kx' < 18.5$, with the bar amplitude equal to the near-bottom excursion amplitude A_b. On each side of this patch, there is an erodible section, $-12.5 < Kx' < 0$ and $18.5 < Kx' < 25$; elsewhere the bed is rigid. At $Kx' = 25$, $B = 0$. At $\bar{t} = 0$, A arrives at $Kx' = -12.5$. At $\bar{t} = 0.02$ (after 0.062 days), four young bars are visible on the sea side ($-12.5 < Kx' < 0$), with the crests under the wave nodes. But in the region $0 < Kx' < 18.5$, each of the old bar crests is midway between an antinode and the next node. As time goes on, the young bars grow higher, and the old bars become smaller. At $\bar{t} = 0.2$ (0.62 days) the height of the old bars are reduced by a factor near 0.7 and equalling that of the young ones. At $\bar{t} = 1.0$ (3.11 days) the old are dwarfed by the young. By $\bar{t} = 5.0$ (15.54 days), the bed is virtually flat and waves are no longer reflected ($\zeta_{env} \simeq 1$). No bars are ever formed on the shoreward side ($18.5 < Kx' < 25$).

12. Comments on related works

In view of the recent research activity on bedforms under waves, comments on two aspects of related studies by others are appropriate. The first is comparing the mechanisms of ripples and bars. The second is on the laboratory simulation of bedforms in nature.

On ripples and bars

It has been shown by Blondeaux (1990) that small-scale ripples are initiated by instability, described mathematically by an eigenvalue problem. Here bars are shown to be formed by a forced diffusion process. The mathematical reason for this difference can be traced to the difference in length scales.

Because the wavelengths of bars and waves are comparable, terms representing convective inertia in the perturbation analysis are $O(\epsilon)$, cf. (5.23). For ripples, however, they are $O(1)$ due to the much shorter ripple wavelength than that of the water waves (Mei & Yu 1997). Momentum transfer across the oscillatory boundary layer is

dominated by viscous diffusion alone for bars, but by both the Reynolds stresses and viscous diffusion for ripples. Mathematically, the leading-order boundary layer flows (ψ_0') of both problems are given by the Stokes solution for an oscillatory flow above a plane bed. However, at the next order (ψ_1'), the bar-induced flow ($\psi_1'^{[1]}$) has only the first harmonics in time, while the ripple-induced flow generates infinitely many time harmonics through the convective inertia. In both cases, the growth rate is proportional to

$$-\frac{\partial}{\partial x'}\left\{\overline{|\psi_0'|^p\left(\psi_1'+\beta\frac{\partial h'}{\partial x'}\right)}\right\} \quad (p>1) \tag{12.1}$$

except for a positive constant factor. Since ψ_0' is sinusoidal in time, $|\psi_0'|^p$ has only even time harmonics, hence its correlations with odd time harmonics of ψ_1' are zero. Thus, for bars the growth rate does not depend on the bar-induced flow $\psi_1'^{[1]}$ and the forcing term $-(\partial/\partial x')(\overline{|\psi_0'|^p\psi_1'})$ is independent of h'. Consequently, the bar evolution equation is inhomogeneous in the unknown bar height. For ripples, the forcing term $-(\partial/\partial x')(\overline{|\psi_0'|^p\psi_1'})$ is contributed by all the even time harmonics of the ripple-induced flow, as part of ψ_1', hence it is proportional to the ripple height as well the slope term. As a result, the evolution equation of ripples is homogeneous in the unknown, and gives rise to an eigenvalue problem and instability.

On laboratory simulation

O'Hare & Davies (1990, 1993) used a flume 10 m long and 0.3 m wide with water depth of 0.15 m. With natural beach sand of diameter $d = 0.28$ mm, the observed ripples were typically 2 cm in height (crest to trough), while the bars were only 3–4 cm. In Rey *et al.* (1995), the flume was even smaller. With sand size of $d = 0.08$ mm, the observed ripple height was 0.23 cm, while the bar height was only 0.5–0.7 cm. In both experiments, sediments were largely transported in suspension and strongly influenced by shedding vortices. This contributed to the shifting of bar crests away from the nodes of the wave envelope, as observed by O'Hare & Davies (1990). In contrast, acoustic sounding records by Dolan (1983) of natural bars in Chesapeake Bay do not show such prominence of ripples. Guided by previous theories, Yu (1999) has reasoned that to ensure dynamical similarity between the laboratory and nature requires that $(A_b\omega)_{lab} = (A_b\omega)_{nature}$ for ripples, which is easy to satisfy. However for sand bars it is necessary that

$$(Kd)_{lab} \simeq (Kd)_{nature}. \tag{12.2}$$

For a typical ratio of wavelengths of 1 to 50, the model sand must be $\frac{1}{50}$ the size of the natural sand, which is very difficult to achieve. Therefore the relative prominence of ripples in recent laboratory tests with natural sand is largely exaggerated; for better simulations of sand bars in nature, or more definitive checks of our theory, it is necessary to use large flumes.

13. Concluding remarks

Under the assumptions that waves, bars and ripples are all gentle in slope, we have coupled simple models of bedload sediment transport and wave-induced fluid flow to examine the mechanics of sand bar evolution. For a sand bed in a constant mean water depth, several main conclusions have emerged. First, sand bars form via a process of forced diffusion. Diffusivity is provided by gravity and affected by the

local shear stress, while forcing is caused by the second-order fluid flow field in the boundary layer. Owing to the nonlinearity of sediment dynamics, both the mean flow (Eulerian streaming) and the second time harmonic contribute to the forcing. Second, finite reflection from the shore is both necessary and sufficient for the formation and maintenance of sand bars; the presence of mean circulation cells is not a prerequisite. If all other factors are equal, stronger shore reflection leads to higher bars. Third, Bragg scattering causes two concurrent physical processes: (1) energy transfer between two wavetrains propagating in opposite directions; (2) change of surface wavelength. Both processes are determined by the position of bar crests relative to wave envelope nodes.

We have also extended our model to the case of horizontally varying eddy viscosity which increases with the local orbital amplitude. The results are qualitatively similar, and will be described elsewhere. In future development of theoretical models for practical predictions, further improvements are of course needed to take into account at least the following: (i) both bedload and suspended load, (ii) effects of mean bottom slope on the rate of sediment transport, (iii) improvement of turbulence model, (iv) effects of wave nonlinearity including infragravity waves, and (v) effects of the sea spectrum. Owing to the complexity of sediment dynamics, the first task is likely the most challenging, since rational theories for the physics of resuspension and deposition are not yet available. For the second task new experiments on oscillatory flows over an inclined sand surface are needed. The fluid mechanical tools for the remaining tasks exist in principle, and should be applied to help predict one of the most intriguing phenomena of pattern formation in nature.

We gratefully acknowledge the financial support by US National Science Foundation (Grant CTS 9634120 directed by Dr Roger Arndt and Dr John Foss), and Office of Naval Research (Grant N00014-92-J-1754, directed by Dr Thomas Swean).

Appendix A. Estimation of eddy viscosity

For a given wave condition (A_b and ω), we first estimate the ripple height $\Delta\eta$ from the empirical formula of Nielsen (1981):

$$\frac{\Delta\eta}{A_b} = \begin{cases} 0.275 - 0.022\sqrt{\Psi}, & \Psi < 156 \\ 0, & \Psi > 156, \end{cases} \tag{A 1}$$

where $\Psi = (A_b\omega)^2/(s-1)gd$. Thus under strong waves, ripples are washed out and sheet flow occurs. Nielsen (1992) suggested that an empirical formula for steady sheet flows due to Wilson (1989), $k_n = 5\Theta d$, may be used for sheet flows under wave actions if Θ is replaced by $\frac{1}{2}f_w(A_b\omega)^2/(s-1)gd$, where f_w is evaluated by using d as the bottom roughness. If ripples are present the empirical formula of Grant & Madsen (1982) is used to find the bottom roughness:

$$k_n = 4.13\Delta\eta. \tag{A 2}$$

Then the friction factor f_w can be found according to

$$f_w = \exp\left\{7.02\left(\frac{A_b}{k_n}\right)^{-0.078} - 8.82\right\}, \quad 0.2 < \frac{A_b}{k_n} < 10^2, \tag{A 3}$$

$$f_w = \exp\left\{5.61\left(\frac{A_b}{k_n}\right)^{-0.109} - 7.30\right\}, \quad 10^2 < \frac{A_b}{k_n} < 10^4 \tag{A 4}$$

(Madsen 1994). The maximum friction velocity then follows from $u_{*m} = \sqrt{f_w/2}A_b\omega$, which is used in turn to get the depth-dependent eddy viscosity $\nu_e(z) = \kappa u_{*m} z$ (Kajiura 1968; Grant & Madsen 1986), where κ is von Kármán's constant. Finally an averaged (over the boundary layer thickness) constant eddy viscosity can be defined by $\nu = \kappa u_{*m}\delta/2$. Since $\delta = \sqrt{2\nu/\omega}$, we have the constant eddy viscosity,

$$\nu = \frac{1}{2}\frac{(\kappa u_{*m})^2}{\omega}. \tag{A 5}$$

For partially reflected surface waves, the horizontally averaged A_b is used to estimate the eddy viscosity. Two sample calculations are given for the same wave period ($T = 8$ s) and water depth ($H = 7$ m), and the same sand size ($d = 0.4$ mm), but for two different incident wave amplitudes A_0, as follows.

For $A_0 = (25, 50)$ cm, we first calculate $A_b = (32.10, 64.18)$ cm. We then find the ripple height $\Delta\eta = (6.57, 8.64)$ cm from (A 1), and $A_b/k_n = (1.22, 1.86)$, hence $f_w = (0.148, 0.119)$ from (A 3), $u_{*m} = (6.86, 12.28)$ cm and $\nu_t(4.79, 15.36)$ cm^2 s^{-1} from (A 5). The corresponding boundary layer thicknesses are $\delta = \sqrt{2\nu/\omega} = (3.50, 6.26)$ cm.

Appendix B. Approximation for $\bar{q}$

Assuming the expansion $\Theta = T_0 + \epsilon T_1 + \cdots$, we get from (4.7) $T_0 = \Theta_0\psi_{0_{\eta\eta}}$ and $T_1 = \Theta_0\psi_{1_{\eta\eta}} + \beta h_x$. The expansion of the amplitude $\widehat{\Theta}$ can in principle, be obtained from that of Θ as $\widehat{\Theta} = \widehat{T}_0 + \epsilon\widehat{T}_1 + \cdots$, where $\widehat{T}_0 = \Theta_0\widehat{\psi_{0_{\eta\eta}}}$ and $\widehat{T}_1$ is not needed for calculating $\bar{q}$. Let us expand the time factor in q (3.9) first:

$$\left(\frac{\Theta}{\widehat{\Theta}}\right)^2 \mathrm{sgn}\,(\Theta) = \left[\left(\frac{\Theta}{\widehat{\Theta}}\right)^2\right]^{1/2}\frac{\Theta}{\widehat{\Theta}} = \frac{|T_0|T_0}{\widehat{T}_0^2} + \epsilon\left\{\frac{2|T_0|T_1}{\widehat{T}_0^2} - \frac{2|T_0|T_0\widehat{T}_1}{\widehat{T}_0^3}\right\} + \cdots. \tag{B 1}$$

Taking the time-average over a wave cycle and noting that T_0 is sinusoidal in time while all variables with hats are time-independent, we then get

$$\overline{\left(\frac{\Theta}{\widehat{\Theta}}\right)^2 \mathrm{sgn}\,(\Theta)} = \epsilon\frac{2\overline{|T_0|T_1}}{\widehat{T}_0^2} + O(\epsilon^2). \tag{B 2}$$

To calculate the time-averaged transport rate $\bar{q}$, we therefore only need the leading order of Q_s', i.e. (4.10) in dimensionless form. Thus

$$\bar{q} = \epsilon Q_{s0}\frac{2\overline{|T_0|T_1}}{\widehat{T}_0^2}. \tag{B 3}$$

Upon using the expressions of T_0, $\widehat{T}_0$ and T_1, we get

$$\bar{q} = 2\epsilon Q_{s0}\frac{\overline{|\psi_{0_{\eta\eta}}|(\psi_{1_{\eta\eta}} - \frac{\beta}{\Theta_0}h_x)}}{(\widehat{\psi_{0_{\eta\eta}}})^2}. \tag{B 4}$$

REFERENCES

Bagnold, R. A. 1966 An approach to the sediment transport problem for general physics. *Geological Survey Professional Paper* 422-I. Washington, DC.

Belzons, M., Rey, V. & Guazzelli, E. 1991 Subharmonic Bragg resonance for surface water waves. *Europhys. Lett.* **16**, 189–194.

Blondeaux, P. 1990 Sand ripples under sea waves. Part 1. Ripple formation. *J. Fluid Mech.* **218**, 1–17.

Boczar-Karakiewicz, B., Bona, J. L. & Cohen, D. L. 1987 Interaction of shallow-water waves and bottom topography. In *Dynamical Problems in Continuum Physics*, Vol. 4 (ed. J. L. Bona), pp. 131–176. Springer.

Boczar-Karakiewicz, B., Paplinska, B. & Winiecki, J. 1981 Formation of sand bars by surface waves in shallow water. Laboratory experiments. *Polska Akademia Nauk, Inst. Budownictwa Wodnego Gdansk, Rozpr. Hydrotech.* **43**, 111–125.

Carter, T. G., Liu, L.-F. P. & Mei, C. C. 1973 Mass transport by waves and offshore sand bedforms. *J. Waterways, Harbors, Coastal Eng. Div. ASCE* **99**, 165–184.

Davies, A. G. & Heathershaw, A. D. 1984 Surface wave propagation over sinusoidally varying topography. *J. Fluid Mech.* **144**, 419–443.

Davies, A. G. & Villaret, C. 1999 Eulerian drift induced by progressive waves above rippled and very rough beds. *J. Geophy. Res.* **104**, 1465–1488.

Dolan, J. T. 1983 Wave mechanisms for the formation of multiple longshore bars with emphasis on the Chesapeake Bay. Masters Thesis, Department of CE, University of Florida.

Evans, O. F. 1940 The low and ball of the eastern shore of Lake Michigan. *J. Geol.* **48**, 476–511.

Fredsøe, J. 1974 On the development of dunes on erodible channels. *J. Fluid Mech.* **64**, 1–16.

Fredsøe, J. & Deigaard, R. 1992 *Mechanics of Coastal Sediment Transport*. World Scientific.

Grant, W. D. & Madsen, O. S. 1982 Movable bed roughness in unsteady oscillatory flow. *J. Geophys. Res.* **87**, 469–481.

Grant, W. D. & Madsen, O. S. 1986 The continental-shelf bottom boundary layer. *Ann. Rev. Fluid Mech.* **18**, 265–305.

Hara, T. & Mei, C. C. 1987 Bragg scattering of surface waves by periodic bars: theory and experiment. *J. Fluid Mech.* **178**, 221–241.

Heathershaw, A. D. 1982 Seabed-wave resonance and sand bar growth. *Nature* **296**, 343–345.

Herbich, J. B., Murphy, H. D. & Van Weele, B. 1965 Scour of flat sand beaches due to wave action in front of sea walls. *Coastal Engineering, Santa Barbara Specialty Conference*, pp. 705–727. ASCE.

Kajiura, K. 1968 A model of the bottom boundary layer in water waves. *Bull. Earthquake Res. Inst.* **46**, 75–123. Disaster Prevention Res. Inst., Tokyo Univ.

Keulegan, G. H. 1948 An experimental study of submarine sand bars. *Beach Erosion Board Tech. Memo. Rep.* 3 US Army Corps Engrs. Reprinted in *Spits and Bars* (ed. M. L. Schwarz). Dowden, Hutchinson & Ross (1972).

Kindle, E. M. 1936 Notes on shallow water sand structures. *J. Geol.* **44**, 861–869.

Kirby, J. T. 1986 A general wave equation for waves over rippled bed. *J. Fluid Mech.* **162**, 171–186.

Lau, J. & Barcilon, A. 1972 Harmonic generation of shallow water waves over topography. *J. Phys. Oceanogr.* **2**, 405–410.

Lau, J. & Travis, B. 1973 Slowly varying Stokes waves and submarine longshore bars. *J. Geophys. Res.* **78**, 4489–4498.

Liu, P. L.-F. 1987 Resonant reflection of water waves in a long channel with corrugated boundaries. *J. Fluid Mech.* **179**, 371–381.

Longuet-Higgins, M. S. 1953 Mass transport in water waves. *Phil. Trans. R. Soc. Lond.* A **245**, 535–581.

Madsen, O. S. 1994 Spectral wave-current bottom boundary layer flows. *Proc 24th Intl Conf. Coastal Engng, Kobe, Japan*, pp. 384–398. ASCE.

Mei, C. C. 1985 Resonance reflection of surface water waves by periodic sand bars. *J. Fluid Mech.* **152**, 315–337.

Mei, C. C. & Ünlüata, Ü. 1972 Harmonic generation in shallow water waves. *Waves on Beaches* (ed. R. E. Meyer), pp. 181–202. Academic.

Mei, C. C. & Yu, J. 1997 Note on the instability of sand ripples under partially standing surface waves. *Phys. Fluids* **9**, 1606–1620.

Nielsen, P. 1979 Some basic concepts of wave sediment transport. *Technical University of Denmark, Institute of Hydrodynamics and Hydraulic Engineering, Series Paper* 20, 160p.

Nielsen, P. 1981 Dynamics and geometry of wave-generated ripples. *J. Geophys. Res.* **86**, 6467–6472.

Nielsen, P. 1986 Suspended sediment concentrations under waves. *Coastal Engng* **10**, 23–31.

Nielsen, P. 1988 Three simple models of wave sediment transport. *Coastal Engng* **12**, 43–62.

Nielsen, P. 1992 *Coastal Bottom Boundary Layers and Sediment Transport*. World Scientific.

O'Hare, T. J. & Davies, A. G. 1990 A laboratory study of sand bar evolution. *J. Coastal Res.* **6**, 531–544.

O'Hare, T. J. & Davies, A. G. 1993 Sand bar evolution beneath partially-standing waves: laboratory experiments and model simulations. *Cont. Shelf Res.* **13**, 1149–1181.

Restrepo, J. M. & Bona, J. L. 1995 Three-dimensional model for the formation of longshore sand structures on the continental shelf. *Nonlinearity* **8**, 781–820.

Rey, V., Davies, A. G. & Belzons, M. 1995 On the formation of bars by the action of waves on an erodible bed: A laboratory study. *J. Coastal Res.* **11**, 1180–1194.

Saylor, J. H. & Hands, E. B. 1970 Properties of longshore bars in the Great Lakes. In *Proc. 12th Conf. Coastal Eng*. Vol. 22, pp. 839–853. ASCE.

Sheppard, F. P. 1950 Longshore bars and longshore troughs. *Beach Erosion Board Tech. Memo.* 15, US Army Corps Engrs. Reprinted in *Spits and Bars* (ed. M. L. Schwarz). Dowden, Hutchinson & Ross (1972).

Short, A. D. 1975 Multiple offshore bars along the Alaskan Arctic Coast. *J. Geol.* **83**, 209–211.

Sleath, J. F. A. 1974 Mass transport over a rough bed. *J. Mar. Res.* **32**, 13–24.

Sleath, J. F. A. 1978 Measurements of bed load in oscillatory flow. *J. Waterway Port Coastal Ocean Engng Div. ASCE* **104**, 291–307.

Sleath, J. F. A. 1982 The suspension of sand by waves. *J. Hydraul. Res.* **20**, 439–452.

Sleath, J. F. A. 1984 *Seabed mechanics*. Wiley.

Sleath, J. F. A. 1991 Velocities and shear stresses in wave-current flows *J. Geophy. Res.* **96**, 15237–15244.

Trowbridge, J. & Madsen, O. S. 1984*a* Turbulent wave boundary layers, 1. Model formulation and first-order solution. *J. Geophy. Res.* **99**, 7989–7997.

Trowbridge, J. & Madsen, O. S. 1984*b* Turbulent wave boundary layers, 2. Second-order theory and mass transport. *J. Geophy. Res.* **99**, 7999–8007.

Van Rijn, L. C. 1993 *Principles of Sediment Transport in Rivers, Estuaries and Coastal Seas*. Aqua Publications.

Vittori, G. & Blondeaux, P. 1990 Sand ripples under sea waves. Part 2. Finite-amplitude development. *J. Fluid Mech.* **248**, 19–39.

Wilson, K. C. 1989 Mobile bed friction at high shear stress. *J. Hydraulic Eng. ASCE* **115**, 825–830.

Yoon, S. B. & Liu, P. L.-F. 1987 Resonant reflection of shallow-water waves due to corrugated boundaries. *J. Fluid Mech.* **180**, 451–469.

Yu, J. 1999 Generation of sand ripples and sand bars by surface waves. PhD thesis, Department of Civil and Environmental Engineering, Massachusetts Institute of Technology.

Yu, J. & Mei, C. C. 2000 Do longshore bars shelter the shore? *J. Fluid Mech.* **404**, 251–268.

Zala Flores, N. & Sleath, J. F. A. 1998 Mobile layer in oscillatory sheet flow. *J. Geophy. Res.* **103**, 12738–12793.